The Astrophysical Journal Letters, 1002:L32 (22pp), 2026 May 10 https://doi.org/10.3847/2041-8213/ae5f8b
© 2026. The Author(s). Published by the American Astronomical Society.
OPEN ACCESS

JWST Unveils a High Mean Molecular Weight Atmosphere for Mini-Neptune TOI-1130 b: Evidence for Formation Beyond the Water Ice Line*

Saugata Barat[1,2], Tyler Fairnington[2,3], Shelby Courreges[4], Chelsea Huang[2], Andrew Vanderburg[1,5,6], Caroline V. Morley[4], Judith Korth[7,8], Hannu Parviainen[9,10], Alexis Brandeker[11], George Zhou[2], Thomas M. Evans-Soma[12], Lizhou Sha[13], Douglas N. C. Lin[14,15], Duncan Wright[2], Ava Morrissey[5], Emma Nabbie[2], Karen A. Collins, Phil Evans[16], Tristan Guillot[17], Keith Horne[18], Don J. Radford[19], Richard P. Schwarz, Avi Shporer[20], Gregorg Srdoc[21], and Olga Suarez[17]

[1] Kavli Institute for Astrophysics and Space Research, Massachusetts Institute of Technology, Cambridge, MA 02139, USA; saugatabarat500@gmail.com
[2] University of Southern Queensland, West Street, Darling Heights, Toowoomba, QLD 4350, Australia
[3] Department of Astronomy & Astrophysics, University of Chicago, Chicago, IL 60637, USA
[4] Department of Astronomy, University of Texas, Austin, TX 78712, USA
[5] Center for Astrophysics | Harvard and Smithsonian, 60 Garden Street, Cambridge, MA 02138, USA
[6] Sloan Research Fellow, USA
[7] Observatoire Astronomique de l'Université de Genève, Chemin Pegasi 51, 1290 Versoix, Switzerland
[8] Lund Observatory, Division of Astrophysics, Department of Physics, Lund University, Box 118, 22100 Lund, Sweden
[9] Departamento de Astrofísica, Universidad de La Laguna (ULL), E-38206 La Laguna, Tenerife, Spain
[10] Instituto de Astrof'isica de Canarias (IAC), E-38200 La Laguna, Tenerife, Spain
[11] Department of Astronomy, Stockholm University, AlbaNova University Center, 10691 Stockholm, Sweden
[12] School of Science, University of Newcastle, Callaghan, NSW, Australia
[13] Department of Astrophysical Sciences, Princeton University, 4 Ivy Lane, Princeton, NJ 08540, USA
[14] Department of Astronomy and Astrophysics, University of California, Santa Cruz, CA 95064, USA
[15] Institute for Advanced Studies, Tsinghua University, Beijing 100086, People's Republic of China
[16] Phil Evans, El Sauce Observatory, Coquimbo Province, Chile
[17] Université Côte d'Azur, Observatoire de la Côte d'Azur, CNRS, Laboratoire Lagrange, Bd de l'Observatoire, CS 34229, 06304, Nice cedex 4, France
[18] SUPA School of Physics and Astronomy, University of St Andrews, North Haugh, St Andrews KY16 9SS Scotland, UK
[19] Brierfield Observatory, Bowral, NSW, Australia
[20] Department of Physics and Kavli Institute for Astrophysics and Space Research, Massachusetts Institute of Technology, Cambridge, MA 02139, USA
[21] Kotizarovci Observatory, Sarsoni 90, 51216 Viskovo, Croatia
Received 2026 February 17; revised 2026 April 10; accepted 2026 April 10; published 2026 May 5

Abstract

We present the combined JWST/NIRSpec/G395H and NIRISS/SOSS transmission spectrum of a warm mini-Neptune, TOI-1130 b (3.66 $R_\oplus$, 19.8 $M_\oplus$, and $T_{\rm eq} \sim 825$ K). It is part of a rare and unique multiplanet system, TOI-1130, which hosts an inner mini-Neptune and an outer hot Jupiter locked in a 2:1 mean motion resonance. From the transmission spectrum of TOI-1130 b we detect multiple molecules—H_2O (7.5σ), CO_2 (3.3σ), and SO_2 (3.6σ), as well as a tentative detection of CH_4 ($\sim 2\sigma$). We find a strong optical slope in the NIRISS/SOSS spectrum, which is consistent with TESS and CHEOPS transit depth measurements. From equilibrium chemistry retrievals we measure the atmospheric metallicity ($\log Z/Z_\odot = 1.8^{+0.4}_{-0.3}$) and C/O ratio ($<0.75$ at 3σ level confidence) and constrain the atmospheric mean molecular weight, $\mu = 5.5^{+1.3}_{-0.8}$ amu. These constraints are consistent with self-consistent forward model grids. We detect no significant He I 1.083 μm absorption signal and find a mass-loss rate upper limit of 10^{11} g s^{-1}. The volatile-rich high mean molecular weight atmosphere of TOI-1130 b along with the "pebble-filtering" effect of the outer hot Jupiter supports the ex situ formation scenario beyond the water ice line and subsequent migration, coherent with its present orbital architecture. A volatile-rich formation scenario could also potentially explain the location of TOI-1130 b at the edge of the "radius cliff." This result hints that the mini-Neptune population may not have a homogeneous formation history; rather, volatile-rich ex situ formation also contributes to its population.

Unified Astronomy Thesaurus concepts: Exoplanet atmospheric composition (2021); Exoplanet formation (492); Mini Neptunes (1063); Transmission spectroscopy (2133)

Materials only available in the online version of record: data behind figure

1. Introduction

The first detection of a hot Jupiter, 51 Pegasi b (M. Mayor & D. Queloz 1995), occurred more than 3 decades ago, yet we do not understand their formation history (R. I. Dawson & J. A. Johnson 2018; J. J. Fortney et al. 2021). Several theories have been suggested: formation beyond the ice line and inward migration due to high-eccentricity migration (Y. Wu & N. Murray 2003; S. Chatterjee et al. 2008; S. Naoz 2016), or disk-driven migration (D. N. C. Lin et al. 1996; S. Ida & D. N. C. Lin 2008), as well as in situ formation

* This study uses CHEOPS data observed as part of the Guaranteed Time Observation (GTO) programme CH_PR149003.

Original content from this work may be used under the terms of the Creative Commons Attribution 4.0 licence. Any further distribution of this work must maintain attribution to the author(s) and the title of the work, journal citation and DOI.

(K. Batygin et al. 2016). However, assembling a large core to facilitate core accretion (J. B. Pollack et al. 1996) close to the host star is challenging due to the lack of available solids (H. E. Schlichting 2014; E. J. Lee & E. Chiang 2016; A. Johansen & M. Lambrechts 2017).

It has been proposed that atmospheric chemical composition can be used to infer formation location within the protoplanetary disk (K. I. Öberg et al. 2011; N. Khorshid et al. 2022; A. B. T. Penzlin et al. 2024), and thus test planet formation theories. However, several degeneracies exist, such as uncertainty about the disk's chemical composition and planet formation processes (P. Mollière et al. 2022; A. D. Feinstein et al. 2025, and references therein). Therefore, it is necessary to calibrate the correlation between planet formation location and atmospheric chemical composition.

We know of certain systems for which the formation history is well constrained. For example, a handful of hot Jupiters (<10 day period) have been discovered which have inner companions (J. C. Becker et al. 2015; C. X. Huang et al. 2020a; L. Sha et al. 2023). Typically, hot Jupiters are not found with inner companions (C. Huang et al. 2016), and this has been interpreted as evidence for high-eccentricity migration where inner planets are scattered out of the system (A. J. Mustill et al. 2015; R. I. Dawson & J. A. Johnson 2018). Therefore, multiplanet systems with an inner planet and an outer hot Jupiter are rare: only ∼7% of systems with hot Jupiters have inner companions (L. Sha et al. 2026), highlighting their rarity. These systems are most likely to be a product of formation through disk-driven migration. These systems with their well-constrained formation history are ideally suited to test the correlation between planet formation location and atmospheric composition.

In this Letter we present the first results from the JWST program GO 3385, which aims to address the questions outlined in the last paragraph by characterizing and comparing the atmospheres of two planets in the TOI-1130 system (C. X. Huang et al. 2020a). TOI-1130 is a multitransiting system with an inner mini-Neptune-sized planet, TOI-1130 b ($3.66 \pm 0.04\ R_\oplus$, $19.8 \pm 0.03\ M_\oplus$, and a 4.07 day period), and an outer hot Jupiter, TOI-1130 c ($13 \pm 0.4\ R_\oplus$, $336 \pm 5\ M_\oplus$, and a 8.35 day period). The parameters of the system have been determined using photodynamical models (L. Borsato et al. 2024; J. Korth et al. 2023). The TOI-1130 system is in a 2:1 mean motion resonance and exhibits transit timing variations (TTVs) of the order of 2 hr (J. Korth et al. 2023). This indicates that the system likely formed through migration from beyond the ice line (C. Beaugé et al. 2006), which results in the capture of the two planets in the 2:1 resonance configuration. Therefore, the orbital configuration and resonance strongly favors formation beyond the ice line and inward migration driven by the disk for both planets.

This Letter particularly focuses on the inner mini-Neptune, TOI-1130 b. It is a warm mini-Neptune (825 K equilibrium temperature assuming an albedo of 0.1) lying at the edge of the "radius cliff." The radius cliff is a feature in the radius–period diagram where the occurrence rate drops off sharply for planets larger than $3\ R_\oplus$ (B. J. Fulton et al. 2017; D. C. Hsu et al. 2019; A. Dattilo et al. 2023) with orbital periods smaller than 100 days. The existence of the radius cliff is predicted by several early evolution models including photoevaporation (J. E. Owen & A. P. Jackson 2012; J. E. Owen & Y. Wu 2013, 2017), core-powered mass loss (S. Ginzburg et al. 2018; A. Gupta & H. E. Schlichting 2019; J. E. Owen & H. E. Schlichting 2024), and/or boil-off (J. E. Owen & Y. Wu 2016). However, recent studies have shown that atmospheric escape processes alone cannot adequately explain the observed shape of the cliff (A. Dattilo & N. M. Batalha 2024) and additional factors such as different formation pathways (R. Burn et al. 2024; A. Chakrabarty et al. 2026) or core-mass distributions (E. J. Lee & J. E. Owen 2025) may play a role. TOI-1130 b lies in a relatively rare part of the period–radius parameter space, which makes TOI-1130, with its already unique architecture, a one-of-a-kind system. The presence of the outer hot Jupiter beyond the orbit of TOI-1130 b ensures that inflowing volatile-rich material from beyond its orbit is blocked due to "pebble filtering" by the hot Jupiter (B. Bitsch et al. 2021; A. D. Schneider & B. Bitsch 2021). Although the efficiency of pebble filtering depends on the mass of the giant planet and diffusion strength (Z. Zhu et al. 2012; B. Bitsch et al. 2018), for solar system models with a proto-Jupiter it has been shown to be efficient (T. Haugbølle et al. 2019), and observations of transitional disks have shown that grain growth in the inner disk becomes inefficient once pebbles have been blocked (B. J. Norfolk et al. 2021). Therefore, we can assume that the chemical composition of the gas and solids which TOI-1130 b would accrete only dependent on the location of accretion within the disk.

The Letter is organized as follows: Section 2 presents the observations, Section 3 the data analysis, Section 4 the key results, and Section 5 the discussion. We summarize and conclude our interpretations in Section 6.

2. Observations

2.1. TESS and CHEOPS

We used 12 Characterising Exoplanet Satellite (CHEOPS) transit observations of TOI-1130 b in total. These transits are from a GTO of CHEOPS (W. Benz et al. 2021), consisting of light curves published by L. Borsato et al. (2024).[22] In addition, CHEOPS observed one transit of TOI-1130 b simultaneously with a JWST/NIRISS/SOSS transit as part of the Simultaneous Exoplanet Observations with JWST program (Program ID CH_PR149003, PI: A. Brandeker). Because TOI-1130 is relatively faint for CHEOPS, we processed the data using the point-spread function (PSF) Imagette Photometric Extraction (PIPE) pipeline developed for CHEOPS (A. Brandeker et al. 2024) as used in A. Brandeker et al. (2022) instead of the Data Reduction Pipeline (S. Hoyer et al. 2020). PIPE employs a principal component analysis (PCA) approach to construct a PSF template library from the image series. The individual PSFs in each frame are then fitted with the derived principal components and a constant background term to measure the target flux.

We made use of 20 TESS transits from Sectors 13, 27, 67, and 94. We use the highest-cadence TESS Presearch Data Conditioning light curves (J. C. Smith et al. 2012; M. C. Stumpe et al. 2012, 2014) when available, otherwise we use the QLP full-frame image (FFI) light curves (C. X. Huang et al. 2020b, 2020c). Two of the additional TESS transits overlaps with TOI-1130 c. They are also excluded from our analysis.

[22] One of the additional CHEOPS transits from L. Borsato et al. (2024) overlaps with TOI-1130 c, which is excluded from our analysis.

2.2. Refining the Transit Timing Solution

TOI-1130 b is the only planet observed by JWST with a transit timing variation amplitude greater than 2 hr, reaching about 5 hr from peak to peak. This required careful planning of the observations. We revised the photodynamical model published by J. Korth et al. (2023) by adding TESS Sector 67 data and new ground-based transit observations from Las Cumbres Observatory (LCO) and Antarctic Search for Transiting ExoPlanets (ASTEP; T. Guillot et al. 2015). The updated model was then used to identify JWST observable transit windows while avoiding overlapping events, and the model's accuracy was validated using ground-based observations obtained before the JWST visit. We also compared our transit predictions with those from L. Borsato et al. (2024), who include CHEOPS, LCO, ASTEP, and TESS data up to Sector 67, and found the two predictions to agree.

2.3. JWST Observations

Two consecutive transits of TOI-1130 b were obtained using JWST/NIRSpec/G395H (2024 August 20) and JWST/NIRISS/SOSS (2024 August 24). The NIRSpec observations were obtained using the default S1600A1 slit, G395H grating, F290LP filter, and the SUB2048 subarray. The NRSRAPID readout mode was used and the observations were taken with eight groups per integrations and a total of 2673 integrations obtained through the 6 hr long visit. For NIRISS/SOSS, we used SUBSTRIP256, which covers all spectroscopic orders and we choose the NISRAPID readout mode. We used two groups per integration and obtained 1320 integrations. The NIRISS visit was also for 6 hr. The number of groups per integration was chosen to ensure that the detector operated in the linear regime. All integrations recorded a flux lower than 60% of the saturation limit of the detector. The JWST data presented in this Letter were obtained from the Mikulski Archive for Space Telescopes (MAST) at the Space Telescope Science Institute. The specific observations analyzed can be accessed via DOI: 10.17909/nzdt-ce06.

3. Data Analysis

3.1. JWST Data Reduction

We begin our analysis from the uncalibrated files (".uncal") for the NIRSpec and NIRISS/SOSS observations. The NIRSpec/G395H images are analyzed using the `Eureka!` data reduction pipeline (T. Bell et al. 2022). `Eureka!` is a widely used and calibrated pipeline, which has been applied to multiple NIRSpec/G395H analyses and benchmarked with other standard data reduction pipelines (e.g., see E. M. May et al. 2023; L. Alderson et al. 2025; S. Barat et al. 2025). We run the first two data reduction stages from `Eureka!`, which wrap the standard `JWST` pipeline functions. We analyze the calibrated Stage 2 outputs from `Eureka!` using `Eureka!` Stage 3 extraction routines. For detailed discussion of the NIRSpec/G395H data reduction see Appendix A.1. We also independently reduced NIRSpec/G395H data using the `exoTEDRF` data reduction pipeline (M. Radica 2024). The two reductions yield consistent results (Figure B1).

We reduce the NIRISS/SOSS images using the `exoTEDRF` data reduction pipeline. `exoTEDRF` is a standard pipeline that has been used for reduction of multiple NIRISS/SOSS time series observations (e.g., see B. Davenport et al. 2025; M. Radica et al. 2025). We follow the standard data reduction steps that are outlined in Appendix A.2. We note that our observations did not include an F277W image, therefore we did not include the order-zero background contamination flagging step. The 1D spectra are extracted using a box extraction.

3.2. JWST Light-curve Analysis

We extract and analyze the transit light curves of TOI-1130 b using custom tools. We used the 1D spectra reduced using `Eureka!` and `exoTEDRF` as discussed in Section 3.1. First, white light curves are extracted by summing over the full wavelength range of the detectors. The white light curves from NIRSpec/G395H NRS1 and NRS2, and NIRISS/SOSS order 1 and order 2 are shown in Figure 1. NRS1 shows a linear slope that has been reported for other similar observations (e.g., L. Alderson et al. 2023; N. Espinoza et al. 2023). NRS2 does not show such a slope. The NIRISS/SOSS light curves do not show any apparent slope, but show a "kink" in the pretransit baseline. Such features have been seen in JWST light curves (e.g., L. Alderson et al. 2023) and could be due to mirror tilt or high-gain antenna (HGA) movement.

We fit the white transit light curves using a linear baseline and a transit model simulated using `batman` (L. Kreidberg 2015). We keep the quadratic limb darkening coefficients, semimajor axis, and midtransit times free for all four white light curves. Other orbital parameters are fixed from L. Borsato et al. (2024). Further details of the white light-curve fitting are described in Appendix B. The residual rms for the white light curve relative to the expected white noise models from `Pandexo` (N. E. Batalha et al. 2017) is 2.1, 1.9, 1.1, and 1.04 for NIRISS order 1, NIRISS order 2, NRS1, and NRS2, respectively. For NIRISS/SOSS we have a likely mirror tilt or HGA movement, which is increasing the rms. Deviation from expected white noise has been reported for white light curves of multiple other JWST datasets (e.g., N. L. Wallack et al. 2024), and are consistent with the white noise rms for the NIRSpec observation.

The spectroscopic light curves are fit at the native resolution of the instruments. We fit the spectroscopic light curves using two approaches: the same model as the white light curve with no additional red noise model and a common-mode correction approach. The details of these methods are outlined in Appendix B. In both cases, the semimajor axis and midtransit time are fixed from the respective white light-curve fits. We note that the semimajor axis from all white light-curve fits are consistent within 1σ. The quadratic limb darkening coefficients are fixed from `Exotic-LD` (D. Grant & H. Wakeford 2024). We note that in the first light-curve fitting approach for NIRISS/SOSS light curves, we trim integrations prior to the kink in the light curve. From this fit we find that the linear baseline slope is wavelength independent for NRS2 and NIRISS order 1 and 2. However, for NRS1 a wavelength dependence is seen that has been reported for previous datasets (e.g., J. T. Sikora et al. 2025).

In the common-mode approach we use a systematics model derived from the white light curve to detrend the spectroscopic light curves (N. P. Gibson et al. 2013; L. Kreidberg et al. 2014; K. B. Stevenson et al. 2014). The systematics model is derived by dividing the observed white light curve with the best-fit transit model. This model assumes that the systematics are wavelength independent, and has been applied to many time series observations, especially with the Hubble Space Telescope (HST; e.g., see L. Kreidberg et al. 2014; S. Barat et al. 2024a).

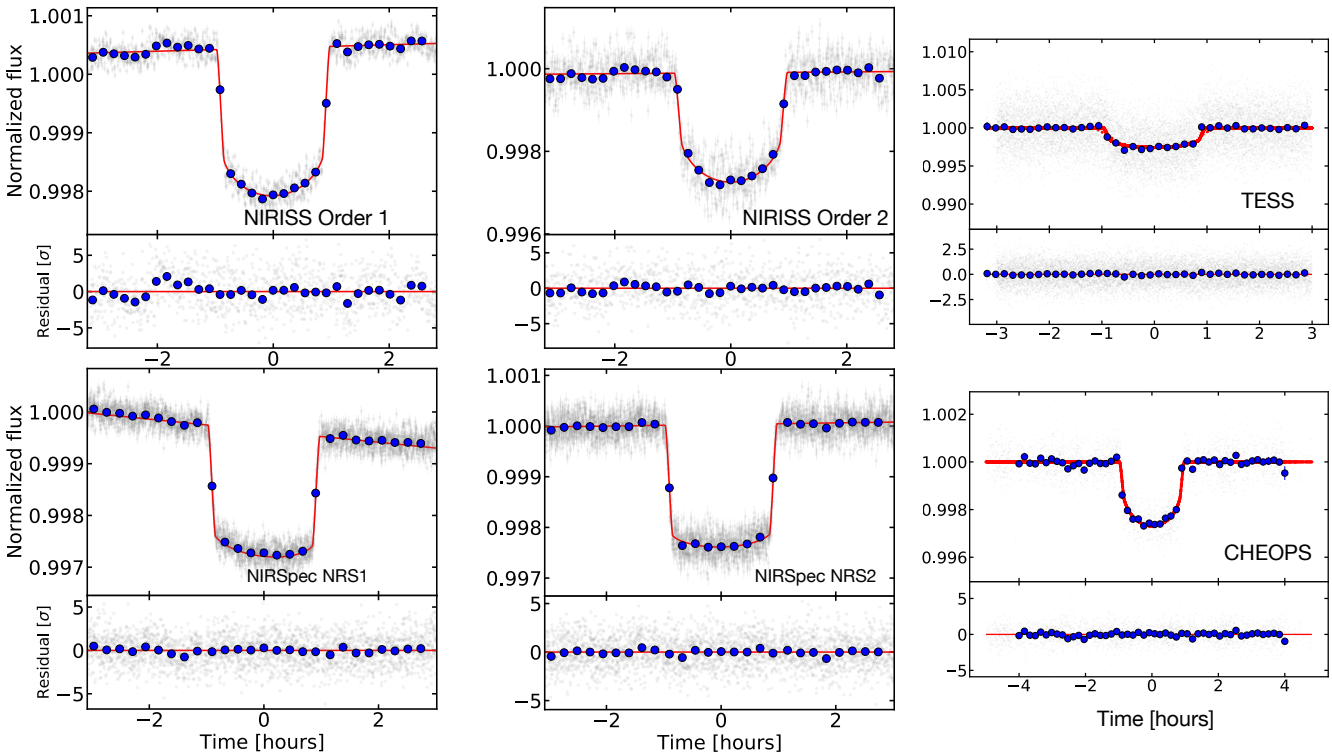


Figure 1. JWST white light curves, and phase-folded TESS and CHEOPS light curves of TOI-1130 b. The upper panel shows NIRISS/SOSS (order 1 on the left and order 2 on the right) and the lower panel shows NIRSpec/G395H light curves (NRS1 on the left and NRS2 on the right). The NIRISS data are reduced using `exoTEDRF` (M. Radica et al. 2025) and the NIRSpec light curves are reduced using `Eureka!` (T. Bell et al. 2022). The details of the data reduction are outlined in Section 3.1. The red solid lines show the best-fit models to the white light curves. The white light curve is fit using a `batman` model with a linear slope and quadratic limb darkening coefficients fixed from `Exotic-LD` (D. Grant & H. Wakeford 2024). We also show 10 minute binned light curves (blue circles). In the NIRISS/SOSS light curves we see a kink before the transit. In NRS1 we see a visit-long slope that has been seen in other observations (N. Espinoza et al. 2023). NRS2 does not show such a slope. We discuss the light-curve fitting methodology in detail in Section 3.2 The right upper panel shows the phase-folded TESS light curve and the lower right panel shows the phase-folded CHEOPS light curve. See Section 3.3 for details of the analysis.

This approach corrects for the kink in the NIRISS spectroscopic light curves. We include a linear slope as a free parameter in the fitting routine for the detrended spectroscopic light curves. For all the detectors the fitted slope in this approach is consistent with zero, but for NRS1 it shows the expected wavelength dependence. We find that the residuals from the spectroscopic light-curve fits (both approaches) bin down similar to expectations from white noise and the reduced χ^2 is consistent with one for all spectroscopic light-curve fits. The transmission spectra derived using both of these light-curve fitting techniques are consistent within 1σ for all spectroscopic light curves (Figures B2, B3). The final transmission spectra are obtained by binning the native-resolution transmission spectra. We use 50 pixel bins for NIRISS order 1, NRS1, and NRS2. For NIRISS order 2 we use two spectroscopic channels. The choice of binning is discussed in detail in Appendix B. The combined JWST transmission spectrum derived from the common-mode correction method for TOI-1130 b is shown in Figure 2. We use this spectrum for the rest of the analysis.

3.3. TESS and CHEOPS Light-curve Analysis

We jointly fit all CHEOPS and TESS data with JWST white light curves from NIRISS/SOSS order 1 and NIRSpec NRS1 and NRS2 to provide additional transit depth constraints in the optical. We allow different planet radii for different bands, and share the other planet parameters (inclination and semimajor axis of the planet) between the bands. For the CHEOPS and TESS transits, we fix the LD values using `Exotic-LD` similar to the JWST spectra light-curve analysis, and fix the t_0 values for individual transits based on the updated TTV solutions. The JWST white light curves have free LD and t_0 values. We simultaneously fit the detrending parameters for all datasets. For the CHEOPS data, we use detrended sets following the `pycheops` package (P. F. L. Maxted et al. 2022) with a second-order polynomial; for TESS and JWST data, only a linear fit with time is used for detrending. For the 30 and 10 minute cadence TESS FFI data, we supersample the transit models before comparing to the observational data.

We also attempted different combinations of detrending, prior, and LD choices for the CHEOPS and TESS data fit. We note the overall TESS transit depth does not change depending on these choices. We find that the CHEOPS transit depths show a maximum variation of $\sim$80 ppm between visits (typical uncertainties are $\sim$40 ppm). Therefore, the different CHEOPS visits are consistent within the 2σ level of significance.

4. Results

4.1. Transmission Spectrum of TOI-1130 b

In Figure 2 we show the combined transmission spectrum of TOI-1130 b. We have combined the JWST/NIRSpec/G395H and NIRISS/SOSS transmission spectra (Section 3.2). We also add the TESS and CHEOPS transit depths (Section 3.3) for a complete optical–near-IR spectrum. The spectrum shows

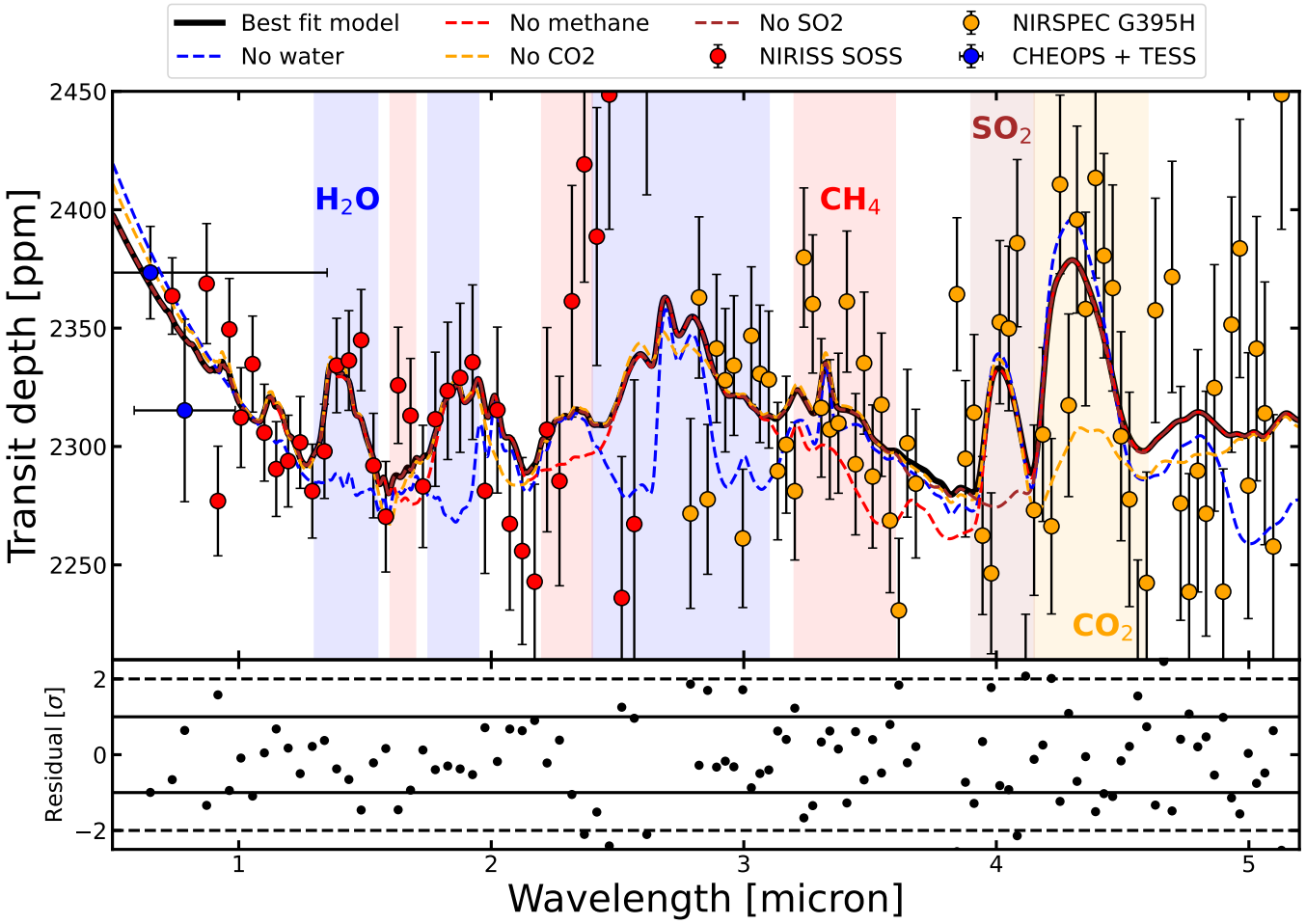


Figure 2. JWST/NIRSpec (orange) and NIRISS/SOSS (red) transmission spectrum of TOI-1130 b. The blue points show the transit depths derived from TESS and CHEOPS discussed in Section 3.3. The derivation of the JWST transmission spectra is discussed in Section 3.2. The error bars shown have been scaled up by the fitted jitter factor. The black solid model shows the best-fit model from a free chemistry retrieval (including error bar scaling) implemented using `PetitRadtrans` (P. Mollière et al. 2019). The best-fit model has a $\chi^2_\nu = 1.01$. The details of the forward model are outlined in Section 4.2. The different colored lines show models where one molecule has been removed from the best-fit model. The vertical dashed regions show the absorption regions corresponding to those molecules. We detect H_2O (7.5σ), CO_2 (3.3σ), and SO_2 (3.6σ), and a tentative detection of CH_4 (2σ). We calculate the detection significances by calculating the difference in χ^2 from the best-fit model and a model where a particular molecule is removed. In Table 1 we show the χ^2 values. The lower panel shows the residuals with respect to the best-fit model. Scaled up error bars have been used to calculate the residuals. The solid and dashed lines show the 1σ and 2σ confidence levels. The JWST/NIRSpec and NIRISS/SOSS spectra are available as the data behind the figure.

(The data used to create this figure are available in the online article.)

several features: we see absorption bumps around 1.4, 1.8, and 3 μm that coincide with water absorption bands (marked with vertical shaded regions in Figure 2). Along with these, we find absorption bumps around 4 and 4.3 μm that are coincident with SO_2 and CO_2 absorption features, respectively. In the optical we find a large slope with NIRISS/SOSS. The transit depths retrieved in SOSS are consistent with the photometric TESS and CHEOPS transit depths.

4.2. Free Retrieval on the TOI-1130 b Transmission Spectrum

We run a free chemistry atmospheric retrieval with the publicly available code `PetitRadtrans` (P. Mollière et al. 2019) on the combined TESS + CHEOPS + JWST spectrum. We include the H_2O, CH_4, CO_2, CO, SO_2, NH_3, HCN, H_2S, and CS_2 mass fractions as free parameters in our forward model. These molecules were chosen as they have dominant absorption features in the wavelength range we probe and have been commonly included in atmospheric free retrievals of mini-Neptunes observed with JWST (e.g., see N. Madhusudhan et al. 2023; T. G. Beatty et al. 2024; B. Benneke et al. 2024; F. E. Rigby et al. 2025). The mean molecular weight of the atmosphere is calculated from the mass fractions of the included species. We assume that the sum of molecular mass fraction equals 1. We assume that the remaining mass fraction is due to H and He and assume a solar H/He ratio. We assume an isothermal atmosphere and include temperature as a free parameter. We fix the mass of the planet to 19.8 $M_\oplus$ (L. Borsato et al. 2024). Since we see a strong slope in the optical part of the transmission spectrum, we add an aerosol opacity, which is modeled by a power law:

$$\kappa_{\rm cloud} = \kappa_0 \, \lambda^\alpha, \tag{1}$$

where the coefficient of the opacity function (κ_0) and the power-law coefficient (α) are included as fit parameters. We include an offset between the NIRISS and NIRSpec spectra (e.g., see N. Madhusudhan et al. 2023). Further details about the forward model are provided in Appendix C.

Table 1
Table Showing the $\delta\chi^2$ and Detection Significance (σ) from Our Free Retrieval with and Without an Added Jitter Term to Account for Residual Red Noise in Our Transmission Spectrum

Model	$\delta\chi^2$ (no jitter)	$\delta\chi^2$ (with jitter)	σ (no jitter)	σ (with jitter)	lnB (Savage–Dickey)	σ (Savage–Dickey)
No H_2O	91	56	9.5	7.5	22.1	6.9
No CH_4	14	7.2	3.7	2.6	2.2	2.6
No CO_2	17	10.7	4.2	3.3	3.8	3.2
No SO_2	15	14	3.9	3.6	5.3	3.6

Note. The $\delta\chi^2$ values are calculated with respect to the best-fit model from the free retrieval and subsequently fixing the abundance of a particular molecule from the model to the lower limit of the uniform priors (10^{-10}). The approximate Bayes factors are calculated using the Savage–Dickey approximation on the posterior distributions. The approximate Bayes factors are converted to a detection significance using the formalism outlined in R. Trotta (2008).

Table 2
Best-fit Parameters from the Free Chemistry Retrieval of TOI-1130 b (See Section 4.2)

Parameter Name	All Data	2.3–2.7 μm Removed	PLATON	T_{eq} = 825 K	With jitter
χ^2_ν	1.8	1.6	1.6	2.36	1.01
[H_2O]	$-0.6^{+0.3}_{-0.5}$	$-0.6^{+0.2}_{-0.5}$	$-0.3^{+0.2}_{-0.5}$	$-0.4^{+0.1}_{-0.2}$	$-0.7^{+0.3}_{-1.1}$
[CH_4]	$-3.5^{+0.5}_{-0.7}$	$-3.6^{+0.6}_{-1.1}$	<-3.5	$-2.5^{+0.4}_{-0.5}$	-4^{+1}_{-2}
[CO]	<-2	<2	<-0.6	<-0.6	<-2
[CO_2]	$-1.2^{+0.6}_{-0.9}$	$-1.1^{+0.5}_{-0.8}$	$-1.8^{+0.7}_{-0.8}$	$-0.7^{+0.2}_{-0.5}$	$-1.2^{+0.6}_{-1.9}$
[SO_2]	$-3.0^{+0.6}_{-0.7}$	$-3.0^{+0.6}_{-0.8}$	$-4.0^{+1.3}_{-1.5}$	$-1.8^{+0.5}_{-0.7}$	$-3.0^{+2.0}_{-1.1}$
[NH_3]	<-2	<-2	<-2	<-2	<-2
R [$R_\oplus$]	$3.65^{+0.01}_{-0.01}$	$3.64^{+0.01}_{-0.01}$	$3.57^{+0.01}_{-0.01}$	$3.64^{+0.01}_{-0.01}$	$3.65^{+0.02}_{-0.02}$
T_{iso} [K]	<600	<600	<600	825 (fixed)	<600
log κ_{cld}	$2.3^{+0.7}_{-0.9}$	$2.5^{+0.8}_{-1.1}$	$3.0^{+0.6}_{-0.6}$	$3.3^{+0.5}_{-0.8}$	$1.4^{+1.0}_{-1.5}$
α	<-4	<-4	<-4	$-9^{+2.4}_{-1.3}$	<3
P_{cloud}	…	…	$5.4^{+1.3}_{-1.4}$	…	…
Offset [ppm]	-8^{+7}_{-7}	-2^{+11}_{-9}	-14^{+7}_{-8}	-25^{+8}_{-9}	-5^{+12}_{-12}
μ [amu]	>3.5	>3.5	>4.4	>3.9	>3

Note. The upper limits correspond to 3σ upper limits. The abundances provided in this table are in mass fraction. μ has been calculated from median values of detected molecular abundances and is interpreted as a lower limit.

From the free retrievals we detect H_2O (9.5σ), CH_4 (3.7σ), CO_2 (4.2σ), and SO_2 (3.9σ). We describe the calculation of detection significance in Appendix C.1. The posterior distributions for CO, HCN, H_2S, and CS_2 do not yield any constraints for these molecules. Although, other molecules, particularly organic molecules, have been included in the retrieval of mini-Neptune JWST spectra (F. E. Rigby et al. 2025; S. Constantinou et al. 2026), we note that the precision of the transmission spectrum in this Letter does not motivate inclusion of further molecular species with weaker features in the forward model. The posterior distribution from the free retrieval is shown in Figure C1. This retrieval does not constrain the isothermal temperature and provides a 3σ upper limit of 600 K. It has often been found that retrieved isothermal temperatures are lower than the expected equilibrium temperature (e.g., see S. Barat et al. 2025; A. W. Mayo et al. 2025), which could be due to averaging of morning and evening terminators (R. J. MacDonald et al. 2020). Furthermore, in a free retrieval the only effect temperature has is to set the size of molecular features through the scale height (J. de Wit & S. Seager 2013). In our models, both the radius at the reference pressure and isothermal temperature are free parameters. However, both can affect the size of molecular features and are therefore correlated, which can be seen in posterior distributions from this retrieval. This could be the reason why we do not constrain the isothermal temperature in the free retrieval, rather we find an upper limit. The free retrieval also finds a strong scattering slope with a 3σ upper limit for the opacity power law of -4. The offset between NIRSpec and NIRISS is consistent with zero. From this fit we calculate a mean molecular weight of 3.5. It is important to note that in the free retrieval the H_2O and CO_2 abundances pushed toward their upper bounds. Therefore, the mean molecular weight we calculate from this free retrieval can be interpreted as a lower limit. The retrieved parameters from this fit are provided in Table 2. We find a reduced χ^2 of 1.81.

Since the reduced χ^2 is higher than one, we redo the free retrieval by including an error inflation ("jitter") term in the likelihood function of our Markov Chain Monte Carlo (MCMC) procedure. Including this term relatively increases the widths of the retrieved abundances. We detect H_2O (7.5σ), CO_2 (3.3σ), and SO_2 (3.6σ) at comparatively lower significance compared to the fit without error inflation. The reduced χ^2 from this fit is 1.01. We also have a tentative detection of methane (2.6σ). However, upon further investigation we found that the detection significance of CH_4 was being increased due to one outlier point at 3.8 μm. When we remove that point from the retrieval the detection significance of CH_4 is reduced to 2σ, while the other molecular abundances and detection

significances do not change significantly. Therefore, we adopt the molecular detection significances from this fit: H_2O (7.5σ), CO_2 (3.3σ), and SO_2 (3.6σ), and a tentative detection of CH_4 (2σ). We verify the detection significances by estimating the Bayes factor by postprocessing the posterior distribution using the Savage–Dickey approximation (J. M. Dickey 1971), and using them to calculate detection significances using the formalism outlined in R. Trotta (2008). We find that the detection significances are consistent with the calculation based on the difference in χ^2.

We find that the red end of the NIRISS detector shows a large scatter and these data points appear as outliers. We test their impact on the retrieval results. We remove data points from 2.3–2.7 μm and rerun the free retrieval using the same setup. We do not include a jitter term for these "test retrievals." The posterior distribution for this is shown in Figure C2 and the best-fit values are shown in Table 2. We find that all the parameters are consistent within 1σ compared to the retrieval on the full dataset. We find a reduced χ^2 of 1.5, which is improved compared to the full dataset fit (without jitter). However, we find that the outliers at the red end of the NIRISS/SOSS detector do not significantly affect the inferred abundances from the observed spectra.

We note that the free retrieval does not constrain the isothermal temperature of the planet, as it pushes it down to very low values ($\sim$300 K). To test the effect of this, we fix the isothermal temperature to the expected equilibrium temperature (825 K) assuming zero bond albedo and full recirculation and run the free retrieval. The posterior distribution and retrieved parameters are shown in Figure C3 and Table 2, respectively. We detect all molecules that were detected using the full retrieval, however, we find a slightly higher abundance for CH_4 and SO_2 ($\sim 2\sigma$ level of significance). We find a higher offset (25 ppm) between NIRISS and NIRSpec compared to previous free retrievals. Water and CO_2 are consistent within the 1σ confidence level. We note that the reduced χ^2 is 2.36, significantly higher than for the full free retrieval. We conclude that the overall conclusion of a metal-rich atmosphere with detections of H_2O, SO_2, and CO_2 remains consistent even if we fix the isothermal temperature.

We perform an independent atmospheric retrieval with free chemistry using the `PLATON` package (M. Zhang et al. 2025) on the combined JWST data only (without the TESS and CHEOPS data points), including the same combinations of molecular species as our `PetitRadtrans` analysis. We generate the opacity sources at a forward model resolution of $R = 20{,}000$. We include an opaque gray cloud deck and power-law haze as our aerosol treatment. The retrieved H_2O, SO_2, and CO_2 abundances are consistent with previous retrievals, while CO, CH_4, and NH_3 are unconstrained. The retrieved opaque gray cloud deck is significantly deeper than 10^3 bar, showing our previous runs with only a power-law opacity source are justified.

From the free retrievals we can conclude that we detect three molecules (H_2O, CO_2, and SO_2) at a detection significance higher than the 3σ confidence level for all the free retrieval setups, and a tentative detection of CH_4 (2σ). We find a strong slope in the optical, which can be explained by a power-law model. Our models find an upper limit to the isothermal temperature ($<$600 K at 3σ), which is lower than the expected equilibrium temperature (825 K) assuming a 0.1 albedo and full redistribution. The retrieved offset between the NIRISS and NIRSpec observations is consistent with zero at a 1σ level of confidence. We postprocess the posterior distributions and calculate mean molecular weight (μ). Assuming the median values of the molecular abundances we calculate a μ of $\sim$3. However, we note that the posterior distributions for water and CO_2 asymptotically increase toward higher values of μ, and we do not constrain the CO abundance. Therefore, we interpret the measured μ as a lower limit.

4.3. Equilibrium Chemistry Retrievals

We run an equilibrium chemistry retrieval using `PetitRadtrans`. All molecules in the free retrieval were included. We note that SO_2, which we detect with our free retrieval, is produced due to photochemistry (S.-M. Tsai et al. 2023), and our equilibrium models do not produce significant amounts of SO_2. However, self-consistent forward model grids have shown that H_2O and CO_2 are not expected to be strongly affected by photochemistry and vertical mixing for high-metallicity atmospheres at the expected temperature of TOI-1130 b (S. Mukherjee et al. 2025). Furthermore, including disequilibrium chemistry in forward models can make them computationally expensive, which is not ideal for a retrieval. Therefore, taking these considerations into account we model the spectrum of TOI-1130 b assuming equilibrium chemistry retrieval. In later sections we will discuss sparse grid models including self-consistent treatment of chemistry to validate the results we report in this section.

We assumed an isothermal atmosphere and include the temperature as a free parameter. We fixed the mass to 19.8 $M_\oplus$ (L. Borsato et al. 2024). The radius at the reference pressure (0.01 bar) is kept as a free parameter. The chemistry is parameterized through the atmospheric metallicity and C/O ratio. The temperature, cloud deck opacity (power-law model), and the offset between NIRISS and NIRSpec are included as free parameters.

From this retrieval we constrain the atmospheric metallicity to $\log Z = 1.92^{+0.5}_{-0.4} \times$ solar and the isothermal temperature to 645^{+146}_{-50} K. The retrieved isothermal temperature is lower than the expected equilibrium temperature assuming zero Bond albedo (825 K) and full recirculation. The C/O ratio is constrained to a 3σ upper limit of 0.75. The retrieved parameters are shown in Table 3. We find a reduced χ^2 of 1.9. Since the reduced χ^2 is higher than one, we rerun our equilibrium chemistry retrieval by including an error inflation term in our likelihood function, similar to the free retrieval case. The posterior distribution from the two fits (no jitter and with jitter) are shown in Figures C4 and C5.

In Figure 3 we show the best-fit model from the equilibrium chemistry retrieval with the error inflation term. The retrieved metallicity ($\log Z/Z_\odot = 1.8^{+0.4}_{-0.3}$) and C/O ratio ($0.2^{+0.4}_{-0.1}$) are consistent with the retrieval without error inflation and the values are shown in Table 3. We adopt these values for the rest of the analysis. We show the retrieved posterior distribution for atmospheric composition and temperature in the same figure. We also show models with solar metallicity, a supersolar C/O ratio (1.0), and a lower isothermal temperature ($\sim$500 K). For temperatures as low as 500 K, equilibrium models underpredict the CO_2 absorption feature at 4.3 μm and can be ruled out at 4σ level of significance. Similarly, low-metallicity ($\sim 10 \times$ solar) atmospheres and supersolar C/O ratio models overpredict CH_4 and underpredict CO_2 absorption features and can be ruled out at a $>5\sigma$ level of significance.

Table 3
Best-fit Parameters from the Equilibrium Chemistry Retrieval of TOI-1130 b (See Section 4.3)

Parameter Name	Free T_{eq}	$T_{eq} = 825$ K	$T_{eq} = 625$ K	Free T_{eq} with jitter
χ^2_ν	1.9	2.3	2.0	1.1
$\log Z/Z_\odot$	$1.9^{+0.5}_{-0.3}$	$2.5^{+0.2}_{-0.2}$	$1.8^{+0.3}_{-0.3}$	$1.8^{+0.4}_{-0.3}$
C/O ratio	$0.2^{+0.3}_{-0.1}$	$0.6^{+0.02}_{-0.02}$	$0.2^{+0.2}_{-0.1}$	$0.2^{+0.4}_{-0.1}$
R [$R_\oplus$]	$3.62^{+0.01}_{-0.01}$	$3.63^{+0.007}_{-0.007}$	$3.61^{+0.007}_{-0.007}$	$3.62^{+0.007}_{-0.007}$
T_{eq} [K]	645^{+146}_{-50}	825	625	608^{+60}_{-30}
$\log \kappa_{cld}$	$3.1^{+0.6}_{-0.9}$	$2.5^{+0.8}_{-1.1}$	$3.0^{+0.6}_{-0.8}$	$2.9^{+0.7}_{-1.0}$
α	$-9.5^{+2.0}_{-1.4}$	$-9.5^{+2.6}_{-1.8}$	$-9.5^{+2.0}_{-1.5}$	$-9.0^{+2.2}_{-1.7}$
Offset [ppm]	-10^{+7}_{-7}	-17^{+7}_{-7}	-13^{+7}_{-7}	-13^{+8}_{-7}
μ [amu]	$5.8^{+1.9}_{-1.1}$	$9.3^{2+.7}_{-2.6}$	$5.4^{+0.9}_{-1.1}$	$5.5^{+1.3}_{-0.8}$

To test the effect of temperature we run two retrievals by fixing the isothermal temperature to 825 K (zero bond albedo) and 625 K (a bond albedo of 0.3). We find that for 825 K, our retrievals converge to a higher atmospheric metallicity ($300^{+200}_{-100} \times$ solar) compared to a free temperature fit (Figure C6). The C/O ratio converges 0.6 ± 0.02 ($\sim$solar). At higher temperatures, subsolar C/O ratios ($\sim$0.2) do not produce methane. Therefore, to account for CH_4 the retrieval converges to a solar value. However, the reduced χ^2 is 2.3 (higher than the free isothermal temperature). For the 625 K retrieval, we find that the retrieved metallicity, C/O ratio, and mean molecular weight are consistent with the free isothermal temperature fit (Figure C7). The reduced χ^2 is two (slightly higher than the free temperature case).

From the equilibrium chemistry retrievals we conclude that TOI-1130 b has a metal-rich atmosphere ($\log Z/Z_\odot = 1.8^{+0.4}_{-0.3}$). We note that the posterior distribution for the C/O ratio falls asymptotically, and we derive a 3σ upper limit of 0.75. We postprocess the retrieved posterior distribution for the equilibrium retrieval with the error inflation term and derived a mean molecular weight of $5.5^{+1.3}_{-0.8}$ amu. We adopt the retrieved parameters from the equilibrium chemistry with the error inflation term for the rest of the analysis.

4.4. Grid Retrievals

We model the transmission spectrum of TOI-1130 b using a self-consistent forward model grid generated with the 1D radiative-convective model PICASO (N. E. Batalha et al. 2019; M. S. Marley et al. 2021; S. Mukherjee et al. 2023) and the chemical kinetics model PHOTOCHEM (N. F. Wogan et al. 2023, 2024) including photochemistry. We generate temperature–pressure profiles and transmission spectra for TOI-1130 b using this setup.

We ran a grid of 27 models testing metallicities of 1×, 10×, and 100 × solar, C/O ratios of 0.3, 1.0, and 2.0, and K_{zz} values of 10^6, 10^{10}, and 10^{13} cm^2 s^{-1}. Within each model, PICASO calculated the temperature structure and radiative transfer, and PHOTOCHEM provided disequilibrium abundances. We first compute a P–T structure with PICASO for each grid model using the system's stellar and planet parameters. Stellar and planetary parameters were taken from L. Borsato et al. (2024): $T_s = 4360$ K, $\log g = 4.55$, [Fe/H] = +0.11, $R_s = 0.697\,R_\odot$, and $M_p = 19.8\,M_\oplus$. We set $T_{eq} = 825$ K and $T_{int} = 50$ K. To match the IR transit depth, we adopt $R_p = 3.55\,R_\oplus$.

Each atmosphere used 91 plane-parallel layers, logarithmically spaced in pressure between 10^5 and 10^{-6} bar. We then ran PHOTOCHEM on the same vertical grid with K_{zz} to include kinetics and photochemistry. We used a MUSCLES UV and optical spectrum for the nearby K dwarf HD 85512. This is not the exact TOI-1130 spectral energy distribution (SED), but it provides realistic UV for photochemistry and haze precursors. We rescaled the MUSCLES spectrum so that the flux at the planet corresponds to $T_{eq} = 825$ K, assuming zero albedo and full redistribution. This way we can model the UV and optical input to the atmosphere consistently. The resulting disequilibrium mixing ratios were passed back to PICASO for the transmission spectrum calculation.

We compare the 27 self-consistent forward model models with the observed transmission spectrum and find that the best-fit model has 100 × solar metallicity, a C/O ratio of 0.3, and $K_{zz} = 10^{10}$ cm^{-2} s^{-1}. The metallicity and C/O ratio values are consistent with the equilibrium chemistry retrievals from `PetitRadtrans` (Section 4.3). We find a reduced $\chi^2 = 3.68$. However, the baseline models did not reproduce the very steep short-wavelength slope. To address this, we tested some modifications, which were applied individually and in combinations, while keeping the P–T structure and baseline composition fixed.

First, within the coupled PICASO and PHOTOCHEM model, we examined the abundances of the sulfur species, including SO_2 observed at 4 μm. Photochemical reactions create layers dominated by SO_2 at 10^{-6}–10^{-4} bar, S_2 at 10^{-4}–10^{-2} bar, with H_2S dominating at deeper layers. The layer we are probing in the transmission spectrum near 4 μm is about 0.06–0.10 mbar. At that layer, H_2S is the dominant sulfur carrier. To fit the observed SO_2 abundance, we increase the sulfur inventory by $\sim$10 by multiplying all S-bearing species by 10 and renormalizing each layer so the mixing ratios sum to 1. The boost raises SO_2 and improves the fit near 4 μm, and we use the boosted spectrum in the model comparison. In the best-fit model, SO_2 reaches a volume mixing ratio (VMR) of 5.17×10^{-5} at the pressures probed by the 4 μm feature.

SO_2 abundance depends strongly on atmospheric metallicity (S. Mukherjee et al. 2025). At temperatures around 800 K SO_2 production is inefficient at solar metallicity (I. J. M. Crossfield et al. 2025). Therefore, the detection of SO_2 in the atmosphere of TOI-1130 b independently shows that it has a high-metallicity atmosphere.

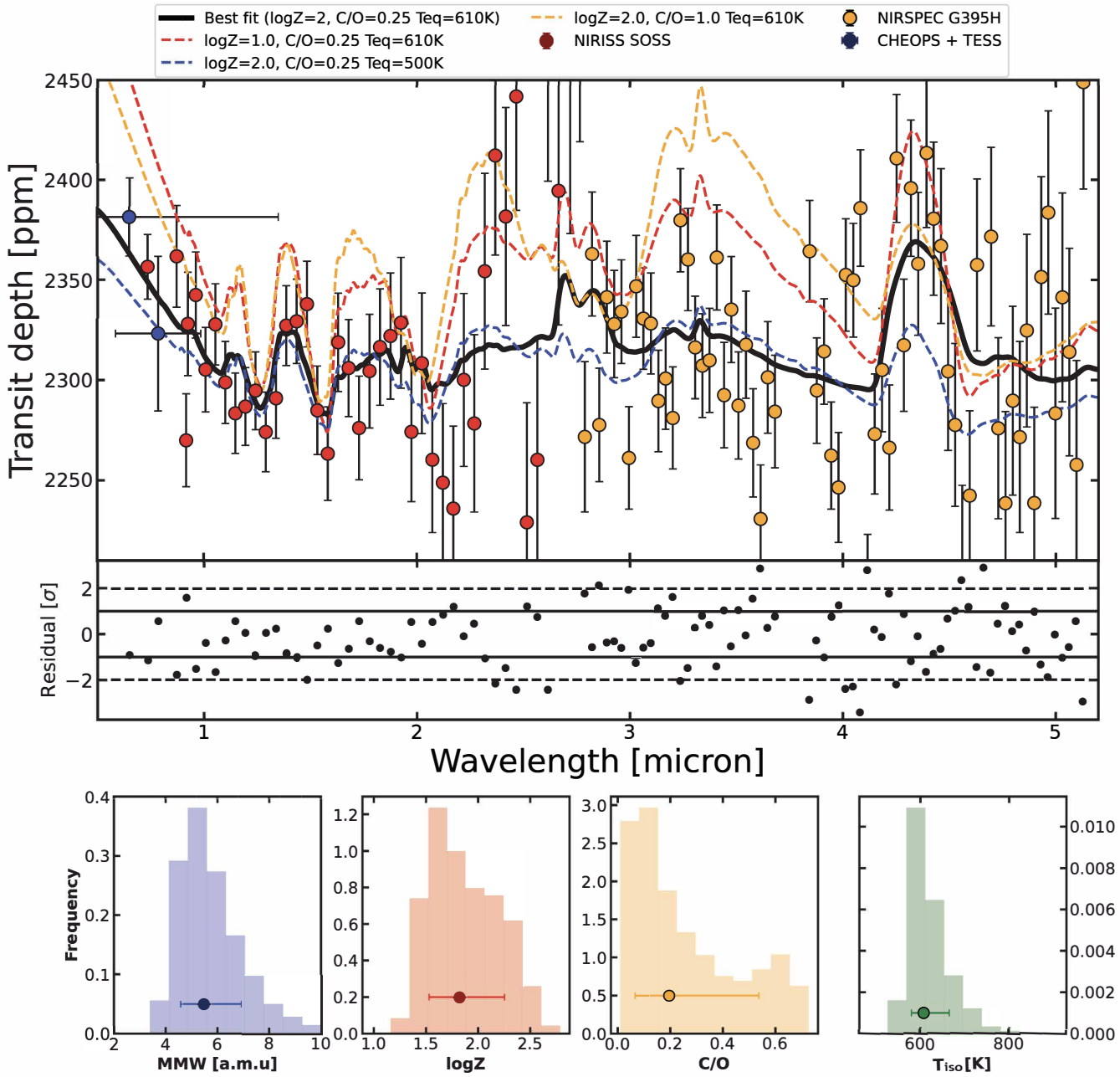


Figure 3. JWST/NIRSpec (orange) and NIRISS/SOSS (red) transmission spectrum of TOI-1130 b. The blue points show the transit depths derived from TESS and CHEOPS discussed in Section 3.3. The derivation of the JWST transmission spectra is discussed in Section 3.2. The error bars shown for the observed spectra have been scaled up by the fitted jitter term from the equilibrium chemistry retrieval. The best-fit model has $\chi^2_\nu = 1.1$. The black solid model shows the best-fit model from an equilibrium chemistry retrieval implemented using `PetitRadtrans` (P. Mollière et al. 2019) including an error inflation term. The details of the forward model are outlined in Section 4.3. The different color models show the effect of varying independent parameters in our forward model. We can rule out a low atmospheric metallicity (∼10), a supersolar C/O ratio (∼1), and a very low isothermal temperature (∼500 K) as they cannot match the CH_4 and CO_2 absorption features. The histograms in the lower panels show the posterior distributions of key retrieved parameters. The mean molecular weight is derived by postprocessing the metallicity and C/O posterior distributions. The best-fit parameters are shown in Table 3.

We also added a Rayleigh-like power law in the upper atmosphere to match the short-wavelength optical slope:

$$\tau_{\rm Rayleigh}(\lambda) = \tau_0 \left(\frac{\lambda}{\lambda_0}\right)^{-\alpha},$$

with $\tau_0 = 0.04$ at $\lambda_0 = 0.5\ \mu$m and $\alpha = 4.5$. We applied this to the top 20 layers setting the single scattering albedo to $\omega_0 \approx 0.999$ and the asymmetry parameter to $g_0 \approx 0$ to add a steep, mostly isotropic scattering slope that matches the observed short-wavelength rise in transit depth. PICASO adds this as an extra scattering opacity in the transmission calculation. With these modifications we could model the optical slope and fit the SO_2 feature better compared to the baseline model. We improve the residual χ^2 to 2.53. This residual χ^2 is comparable to the free chemistry and equilibrium chemistry fits with a fixed (825 K) isothermal temperature. The best-fit model from our grid with scattering and boosted sulfur abundance is shown in Figure 4. We note

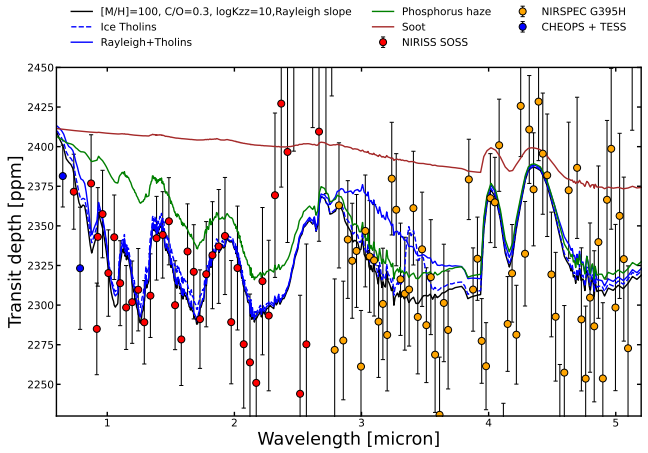


Figure 4. The transmission spectrum of TOI-1130 b observed with JWST/NIRISS and NIRSpec with best-fit models (100 × solar, a 0.3 C/O ratio, and $K_{zz} = 10^{10}$ cm^{-2} gm^{-1}) from the PICASO grid (Section 4.4). A Rayleigh slope and sulfur boost has been added to fit the observations. The best model reduced χ^2 is 2.53. We also different haze models: Titan-like tholins (B. N. Khare et al. 1984), comet-like ice tholins (B. N. Khare et al. 1993), soot (P. Lavvas & T. Koskinen 2017), and Saturn-like phosphorus hazes (N. Noy et al. 1981). A comparison between these models is shown in Table 4.

that the power-law index used for these models is consistent with the upper limit found from the atmospheric retrievals. We also tested models with $\alpha = -4.25$ and -4 and we found that the χ^2_ν did not change significantly.

We also tested different haze slabs with VIRGA (N. E. Batalha et al. 2026). We used a lab size distribution with median radius ∼ 26 nm and a 15–60 nm span (C. He et al. 2018). For each haze sample, VIRGA used the haze specific refractive indices and used `PyMieScatt` (B. J. Sumlin et al. 2018) to compute wavelength-dependent Mie efficiencies and the asymmetry parameter. PICASO mapped these inputs to the per-layer $\tau_{\rm ext}$, ω_0, and g_0 on its cloud grid and computed limb-viewing transmission spectra. We have tested different haze compositions, such as Titan-like reflective tholin hazes (B. N. Khare et al. 1984), which produce a strong feature around 3.3 μm, soot (P. Lavvas & T. Koskinen 2017), which do not reproduce molecular absorption features, Saturn-like phosphorus hazes (N. Noy et al. 1981), and ice tholins, found on icy bodies of our solar system (B. N. Khare et al. 1993). In Table 4 and Figure 4 we compare these different haze models. We find that we can rule out tholin, soot, and phosphorus hazes with high statistical significance (>5σ level of confidence). We also find that a ice-tholins model is worse than the baseline power-law model at 3σ.

4.5. Comparison Between Model Fits to the TOI-1130 b Transmission Spectrum

We have modeled the combined TESS, CHEOPS, and JWST transmission spectrum TOI-1130 b using a free chemistry, equilibrium chemistry retrieval, and a self-consistent forward model grid. We compare the three models in Figure 5. We find that the retrieved free chemistry abundances are consistent with both the equilibrium chemistry and self-consistent forward model grid abundance profiles. We find H_2O (7.5σ), CO_2 (3.3σ), and SO_2 (3.6σ), and a tentative detection of CH_4 (2σ). The free retrieval model and the grid model (including photochemistry) show the SO_2 feature at

Table 4
Comparing the Different Haze Models with the Observed Spectrum of TOI-1130 b

Model	χ^2	Rejection σ=$\sqrt{\Delta\chi^2}$
Baseline + Rayleigh	253	...
Ice Tholins	261	3.09
Tholins	325	8.55
Soot	1199	30.90
Phosphorus	435	13.53

Note. The $\Delta\chi^2$ values are computed with respect to the baseline model, which is used to calculate the rejection significance of the different models. The number of degrees of freedom for each model are the same.

4 μm. Since SO_2 is mainly produced due to disequilibrium photochemistry, our equilibrium chemistry model does not produce observable amounts of SO_2. The retrieval models have been fitted using an error inflation term. The metallicity and C/O ratio we derive from the equilibrium chemistry model and grid model are consistent with each other (∼100 × solar, and a C/O ∼3σ upper limit of 0.75). This results in a μ of $5.5^{+1.3}_{-0.8}$ amu. This is also consistent with the free retrieval, which finds a lower limit of 3 amu. For the free retrieval, the isothermal temperature is low (∼400 K) compared to the equilibrium chemistry retrieval and grid model. Therefore, we find that the width of the 4.3 μm CO_2 feature is smaller in the free retrieval best-fit model. We conclude that considering the differences in all three fitting approaches, all three agree in a metal-rich high mean molecular weight atmosphere.

4.6. Potential He Escape from TOI-1130 b

In Figure 6 we show the transmission spectrum of TOI-1130 b, zoomed in on the 1.083 μm He triplet feature, which has been used as a tracer of atmospheric escape (A. Oklopčić & C. M. Hirata 2018; J. J. Spake et al. 2018). We do not find a significant planetary He absorption feature. We use the formalism outlined in J. Orell-Miquel et al. (2024) to derive the transmission spectrum. We take a 20 pixel half-width region centered on the He line and normalize the stellar 1D spectrum by fitting a straight line. From the continuum normalized spectrum, we calculate the mean in-transit spectrum and mean out-of-transit spectrum.

We compare this spectrum with models calculated using the publicly available `p-winds` code (L. A. Dos Santos et al. 2022). We adopt the stellar SED for HD 85512 from the MUSCLES survey (K. France et al. 2016). We calculate a grid of models assuming two different temperatures of the upper atmosphere (8000 and 10,000 K) and three mass-loss rates (10^9, 10^{10}, and 10^{11} g s^{-1}). We find that for both temperatures high mass-loss rates (10^{11} g s^{-1}) produce a deep He absorption feature and can be ruled out by the observed spectrum.

5. Discussion

5.1. Origin of Volatiles in TOI-1130 b: Accretion Beyond the Water Ice Line

The orbital architecture (inner mini-Neptune and outer hot Jupiter) and the 2:1 mean motion resonance of the TOI-1130 system provide strong hints that this system assembled beyond the water ice line and migrated inward due to disk migration. It

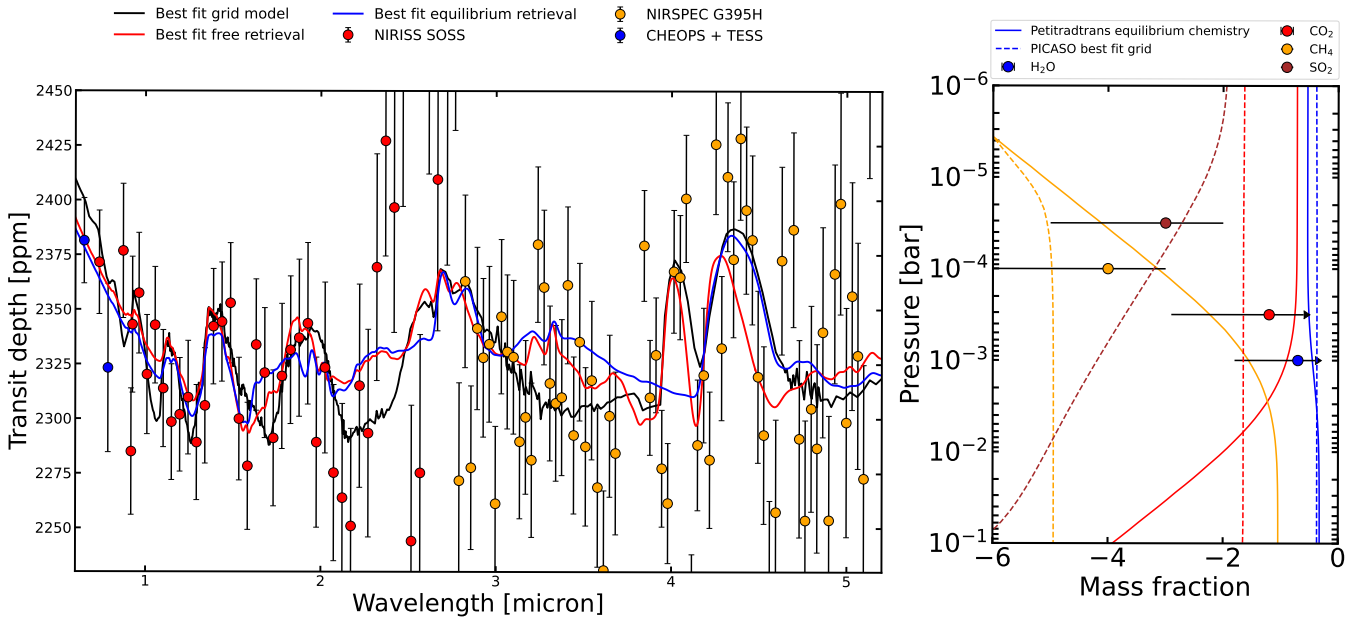


Figure 5. Transmission spectrum of TOI-1130 b with the best-fit free chemistry, equilibrium chemistry, and grid models overplotted (left), and a comparison between the retrieved abundances from the three model fits for TOI-1130 b (right). The points shown in the right panel are the best-fit mass fractions from the free retrieval. The H_2O and CO_2 posterior distributions show lower limits, where as the other molecules show Gaussian distributions. Therefore the H_2O and CO_2 data points are shown with upper arrows. The solid lines show chemical abundance profiles from equilibrium chemistry and the dashed lines show the chemical profiles from the self-consistent forward model grid.

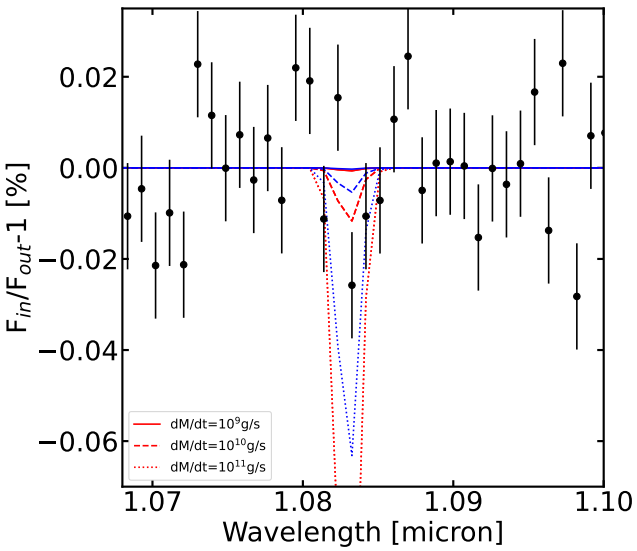


Figure 6. We show the transmission spectrum of TOI-1130 b, zoomed in on the He triplet feature. We derive this spectrum using the formalism described in Section 4.6. The overplotted models have been calculated using the publicly available `p-winds` (L. A. Dos Santos et al. 2022) code. The red lines correspond to an upper atmosphere temperature of 8000 K and the blue lines correspond to 10,000 K models. The different line styles correspond to different mass-loss rates.

has been hypothesized that mini-Neptunes could have originated beyond the ice line and later migrate (S. N. Raymond et al. 2018; J. Venturini et al. 2020; L. Zeng et al. 2021). In this case, the planet would have access to volatile-rich solids that can be accreted to increase the volatile budget of the planet (B. Bitsch et al. 2019, 2021). This would lead to volatile-rich interiors (A. Aguichine et al. 2021) and atmospheres (A. Aguichine et al. 2025).

The high mean molecular weight atmosphere ($5.5^{+1.3}_{-0.8}$ amu) our transmission spectrum has revealed for TOI-1130 b indicates that it is volatile rich: 72% H_2/He and 20% H_2O by mass. This is consistent with formation beyond the ice line and the significant accretion of volatile-rich solids and disk gas rich in H_2/He to form a high mean molecular weight envelope. The disk within the water ice line can be enriched with volatiles due to pebble drift and evaporation (R. A. Booth et al. 2017; A. D. Schneider & B. Bitsch 2021), however due to the presence of the hot Jupiter in the TOI-1130 system, the migrating pebbles would be blocked (B. Bitsch et al. 2021), leaving it volatile poor. Therefore, if TOI-1130 b accreted within the water ice line, it would be difficult to explain its observed atmospheric metal enrichment. Furthermore, it has been shown that in situ formation results in low C/O ratios (M.-L. Steinmeyer et al. 2026), and the detection of both H_2O and CO_2 in TOI-1130 b is consistent with formation beyond the ice line.

TOI-1130 b occupies a rare location in the radius–period diagram: with a radius of 3.66 $R_\oplus$ and an orbital period of ∼4 days, it lies at the edge of the radius cliff with an occurrence rate of <1% (A. Dattilo et al. 2023). One of the leading theories for the formation of mini-Neptunes is the "gas-dwarf scenario" (J. E. Owen & Y. Wu 2013, 2017): in situ formation (E. J. Lee et al. 2014; E. J. Lee & E. Chiang 2016) and subsequent evolution due to mass-loss mechanisms (J. E. Owen & A. P. Jackson 2012; S. Ginzburg et al. 2018). These mechanisms naturally remove a significant amount of H/He from close-in small planets and sculpt them to smaller radii, leading to a dearth of planets larger than 3 $R_\oplus$ and forming the radius cliff. However, recent studies have pointed out that mass-loss processes alone cannot explain the radius cliff (A. Dattilo & N. M. Batalha 2024; E. J. Lee & J. E. Owen 2025) and may require different formation mechanisms, such as formation beyond the ice line and migration (A. Chakrabarty et al. 2026; R. Burn et al. 2024). If

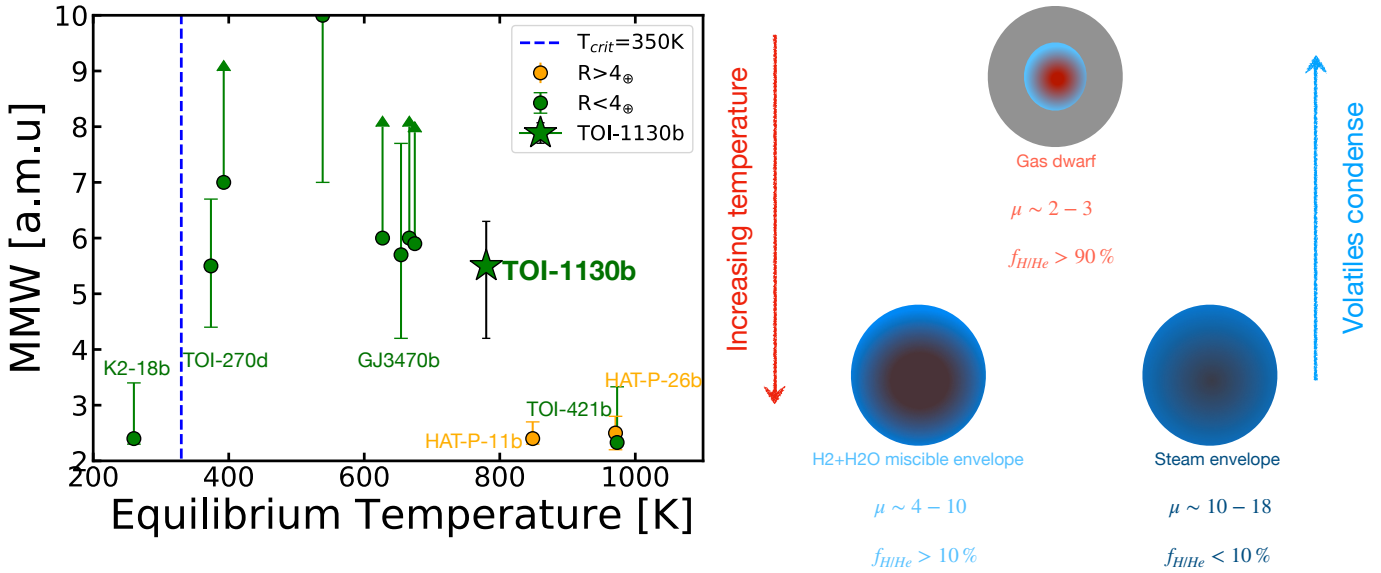


Figure 7. Mean molecular weight (μ) of mini- and super-Neptunes as a function of equilibrium temperature. The μ values are taken from the literature and shown in Table D1. We show TOI-1130 b in this figure. We calculate the mean molecular weight from the posterior distribution of the equilibrium chemistry retrieval (Section 4.3). The blue vertical line marks the critical temperature for the condensation of water (350 K) as proposed in N. Madhusudhan et al. (2025). The schematic on the right demonstrates this idea. Above the critical temperature, the water in the planet is vaporized and mixed with the H/He envelope to form either H_2–H_2O mixed envelopes (miscible envelope mini-Neptunes) or steam-dominated envelopes (steam worlds). The intermediate μ value of TOI-1130 b likely aligns it with the miscible envelope mini-Neptunes.

TOI-1130 b was born with a high mean molecular weight atmosphere, it would not undergo significant atmospheric mass loss (T. Yoshida & E. Gaidos 2025) and would retain its size through its evolutionary phase (J. G. Rogers 2025). This could explain its position in the radius–period diagram. The nondetection of planetary He absorption (Figure 6) is consistent with this. Assuming a mass-loss rate upper limit of 10^{11} g s^{-1}, we calculate that the planet would lose $\sim$0.5 $M_\oplus$ over 1 Gyr, and therefore not undergo significant evolution.

5.2. Alternative Source of Volatiles in TOI-1130 b

Recent studies have shown that interior–atmosphere interactions could have a significant impact on the atmospheric composition of low-mass planets (F. E. Rigby et al. 2024; O. Shorttle et al. 2024; T. Lichtenberg et al. 2025), like mini-Neptunes, as their interior and envelope mass fractions are comparable. For these mini-Neptunes, it has been suggested that global magma oceans can exist at the interior–atmosphere boundary (C. Dorn & T. Lichtenberg 2021), and interactions between the magma and atmosphere can outgas significant amount of volatiles, like water (E. S. Kite et al. 2020). These interactions can affect the metal mass fraction (A. Werlen et al. 2025a) and elemental abundance ratios (A. Werlen et al. 2025b; M.-L. Steinmeyer et al. 2026), which have been traditionally linked to planet formation (K. I. Öberg et al. 2011). For instance, M. C. Nixon et al. (2025) have shown that the volatiles detected in the mini-Neptune TOI-270 d (B. Benneke et al. 2024) can be explained by magma–atmosphere interactions.

However, these models are well suited for low-mass mini-Neptunes. TOI-1130 b, with an estimated envelope mass fraction of 25%, assuming a 15 $M_\oplus$ core, and a high mean molecular weight atmosphere ($\sim$5.5 amu) lies at the transition between low-mass mini-Neptunes and more massive Neptune-like planets. It has been suggested that for planets with high pressure at the interior–envelope boundary, magma is likely to solidify (B. Breza et al. 2025; R. Calder et al. 2025), and cut off interior–atmosphere interactions. Comparing TOI-1130 b with the grids presented in B. Breza et al. (2025), we find that it lies in a region where it is difficult to predict whether it will have a liquid magma ocean. Furthermore, strong vertical mixing is necessary to affect the atmospheric composition of the observable atmosphere, even if magma–atmosphere interactions are happening (A. Werlen et al. 2025b). Therefore, for planets with a high envelope mass fraction, such as TOI-1130 b, current models do not predict how strongly their observable atmospheres can be affected due to these interactions.

5.3. Comparing TOI-1130 b with Mini-Neptunes and Super-Neptunes

TOI-1130 b lies at the edge of the radius cliff: a transition between the smaller mini-Neptunes and the larger and rarer super-Neptunes. In this section, we compare the inferred atmospheric properties of TOI-1130 b with both mini-Neptunes and super-Neptunes.

5.3.1. Mean Molecular Weight

TOI-1130 b has a mean molecular weight of $5.5^{1.3}_{-0.8}$ amu derived from the best-fit retrieval models. In Figure 7 we compare its mean molecular weight with mini-Neptunes and super-Neptunes with a constrained μ from HST and JWST observations. The sample of planets used for this comparison is shown in Table D1. TOI-1130 b has similar μ to mini-Neptunes like TOI-270 d ($\sim$5.5 amu; B. Benneke et al. 2024) and GJ 3470 b ($\sim$6 amu; T. G. Beatty et al. 2024). It has been hypothesized that the atmospheric mean molecular weight is dependent on the temperature (B. Benneke et al. 2024; N. Madhusudhan et al. 2025). Above a critical temperature ($\sim$350 K), water is vaporized and mixes into the atmosphere with lighter gases like H_2 and He. These warm mini-Neptunes

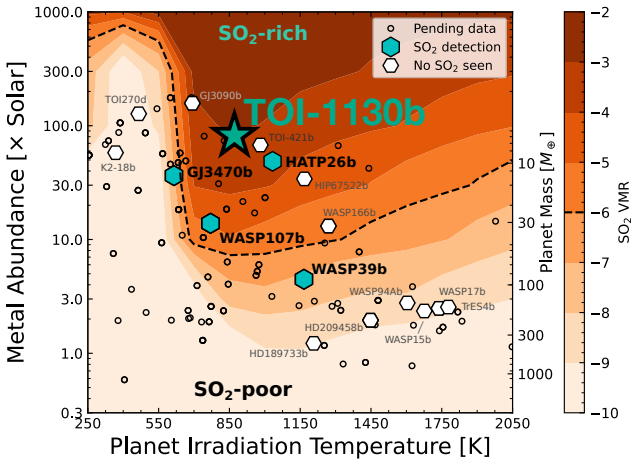


Figure 8. SO_2 abundance as a function of irradiation temperature and atmospheric metallicity (left) adapted from I. J. M. Crossfield et al. (2025). TOI-1130 b joins GJ 3470 b as the second mini-Neptune with a SO_2 detection, and is consistent with a high-metallicity atmosphere.

have been classified as "miscible envelope mini-Neptunes" (B. Benneke et al. 2024). Although TOI-1130 b is more massive than typical mini-Neptunes like TOI-270 d, its atmospheric μ makes it consistent with the miscible envelope scenario. Compared to mini-Neptunes, super-Neptunes like HAT-P-11 b (Y. Chachan et al. 2019) and HAT-P-26 b seem to have low μ atmospheres, comparable to the H/He-dominated atmospheres of gas giants. Therefore, although TOI-1130 b is comparable to HAT-P-11 b (25 $M_\oplus$) and HAT-P-26 b (19 $M_\oplus$) in terms of mass, their atmospheres appear very different (volatile rich versus H/He dominated). With more planets being observed near the radius cliff in the future we will be able to test whether a transition in atmospheric composition truly occurs in this region.

5.3.2. SO_2 Detection in Mini-Neptunes

From the free retrievals we constrain the SO_2 abundance to a mass fraction of 10^{-3} and a VMR of 10^{-4}. In Figure 8 we show TOI-1130 b in the atmospheric metallicity–irradiation temperature plane with SO_2 abundance contours from self-consistent forward model grids that include sulfur photochemistry (I. J. M. Crossfield 2023; I. J. M. Crossfield et al. 2025). TOI-1130 b joins GJ 3470 b (T. G. Beatty et al. 2024) as a second mature mini-Neptune with a detected SO_2 feature.

SO_2 production is strongly dependent on equilibrium temperature and atmospheric metallicity (S. Mukherjee et al. 2025). For TOI-1130 b, the predicted SO_2 abundance is very low for metallicities below 30 × solar. Therefore, the SO_2 detection independently rules out such low-metallicity atmospheres, consistent with our finding from equilibrium chemistry retrievals. We also find that for temperatures below 600 K SO_2 production requires extremely high metallicity (>500 × solar). This is consistent with the nondetections reported for cooler mini-Neptunes, such as TOI-270 d (B. Benneke et al. 2024) and K2-18 b (N. Madhusudhan et al. 2023), and detections for warmer min-Neptunes like GJ 3470 b and TOI-1130 b.

5.3.3. Atmospheric Feature Size as a Function of Temperature

A quadratic temperature-dependent trend has been reported for molecular absorption feature size for mini-Neptunes and super-Neptunes (J. Brande et al. 2024). This trend has been reported based on the 1.4 μm water absorption feature accessible to HST/WFC3. The fitted trend shows that the water feature amplitude size is attenuated between 500 and 700 K.

We reexamine this trend using the sample of mini-Neptunes and super-Neptunes shown in Table D2. We calculate their expected equilibrium temperature assuming an albedo of 0.3 (as assumed in J. Brande et al. 2024). For planets with published JWST transmission spectra, we assume the best-fit value or lower limit on μ from the literature for the calculation. For those planets without a published mean molecular weight we assume 100 × solar metallicity and a solar C/O ratio, which approximately translate to a μ of four. We define the scale height metric in Equation (5.3.3) (J. Brande et al. 2024):

$$A_H \equiv (\delta_{\lambda_0} - \delta_{\lambda_1})(R_*^2/2HR_p).$$

We calculate A_H for the 1.4 μm water band ($\lambda_0 = 1.4$ μm and $\lambda_1 = 1.25$ μm), and for the CO_2 band ($\lambda_0 = 4.3$ μm and $\lambda_1 = 4.15$ μm). δ_λ corresponds to the transit depth at a particular wavelength. The wavelengths in our calculation are chosen such that we compare the center and wings of a molecular feature. For TOI-1130 b we calculate an equilibrium temperature of 780 K (assuming a 0.3 albedo and full recirculation) and a μ of 5.5 amu for this calculation. We find $A_H^{H_2O} = 2.3 \pm 1.3$ and $A_H^{CO_2} = 6.4 \pm 2.1$ for TOI-1130 b. The values and data used for the calculation of A_H for the other planets in the sample are shown in Table D2.

We rederive the quadratic trend by including new JWST observations (Figure 9) that had not been used in J. Brande et al. (2024). We find that if we include data points below 1000 K, the new fit parameters are consistent with the J. Brande et al. (2024) fit within 2σ, however, if we include planets hotter than 1000 K, we find a much weaker quadratic trend. The quadratic term is consistent with zero. TOI-1130 b is consistent with the quadratic $A_H^{H_2O}$ trend presented in J. Brande et al. (2024) as well as the new fit we derive. We do not find a significant trend for $A_H^{CO_2}$. We find that a flat line fit for $A_H^{CO_2}$ gives $\chi^2_\nu = 1.07$ whereas a quadratic fit gives 1.4. The $A_H^{H_2O}$ trend seems consistent with both mini-Neptunes and super-Neptunes cooler than 1000 K.

One of the potential explanations for the quadratic $A_H^{H_2O}$ trend is the presence of photochemical hazes (P. Gao et al. 2020). Haze production becomes efficient at temperatures around 600 K due to increasing methane abundance (P. Gao & X. Zhang 2020; J. J. Fortney et al. 2020) and decreases with increasing temperature (C. He et al. 2018). At low temperatures (<400 K) lab experiments have shown that haze production could decrease (X. Yu et al. 2021). Haze opacity decreases at longer IR wavelengths (Y. Kawashima & M. Ikoma 2018). Therefore, the 4.3 μm CO_2 feature could be less attenuated compared to the 1.4 μm water feature, which is consistent with the nondetection of a trend for $A_H^{CO_2}$. It has been predicted that for equilibrium temperatures higher than 950 K the aerosol opacity is dominated by silicate (SiO_2) condensation (P. Gao et al. 2020). Silicate clouds have been detected for hot Jupiters (D. Grant et al. 2023; J. Inglis et al. 2024) and directly imaged planets (B. E. Miles et al. 2023; K. K. W. Hoch et al. 2025) in the temperature range of 1000–1500 K. We find that including planets with a

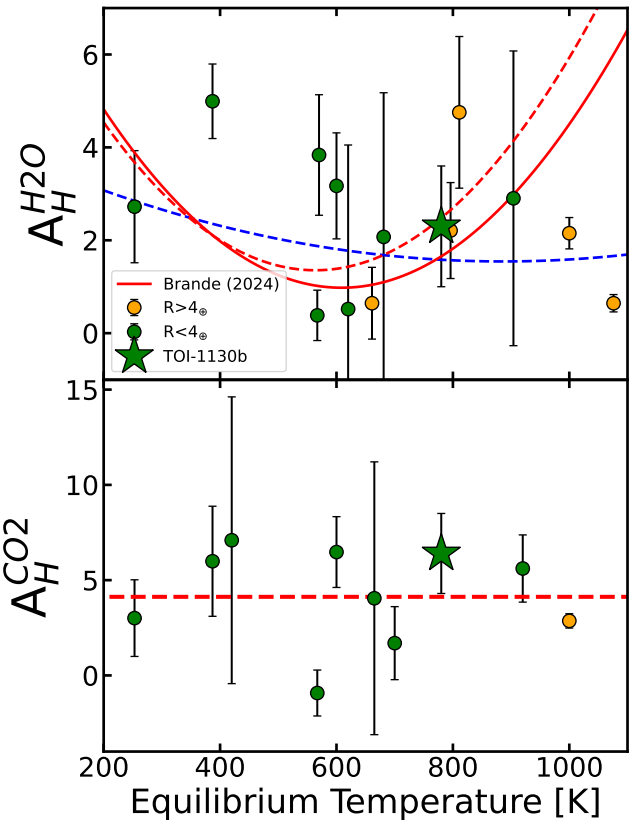


Figure 9. Scale height metric (Equation (5.3.3)) for mini- and super-Neptunes as a function of temperature. The upper panel is the water band at 1.4 μm and the lower panel is the CO_2 band at 4.3 μm. We show TOI-1130 b in this diagram with $A_H^{H_2O} = 2.3 \pm 1.3$ and $A_H^{CO_2} = 6.4 \pm 2.1$ assuming a μ of 5.5 amu. We overplot the tentative quadratic trend reported in J. Brande et al. (2024) for $A_H^{H_2O}$ using only HST data (red solid line). We refit a quadratic function with the JWST data points included and it gives a trend consistent with J. Brande et al. (2024) if we do not include data points beyond 1000 K (red solid line). Including the two points after 1000 K finds a weaker quadratic fit (blue dashed line). The flat dashed line in the lower panel shows the best-fit flat line to the sample. The temperatures used in this plot have been calculated assuming an albedo of 0.3 and full recirculation. The data used to generate this figure are shown in Table D2.

temperature higher than 1000 K weakens the quadratic trend in the water band. Interestingly, the only data point in our sample that is higher than 1000 K and has a CO_2 feature also lies below the best-fit trend. This could potentially be due to the formation of silicate clouds at temperatures around 1000 K, which would have an effect on both bands discussed here. Therefore, at temperatures around 1000 K we could see a transition between the dominant aerosol composition from hazes to clouds, and clouds would attenuate the molecular features across all wavelengths, unlike hazes that affect blue wavelengths more. However, we note that the sample size of planets is small and we need future JWST observations in this parameter space to confirm this potential trend.

6. Summary and Conclusions

In this Letter we present the transmission spectrum of TOI-1130 b (3.66 $R_\oplus$, 19.8 $M_\oplus$, and 825 K) observed using JWST/NIRISS/SOSS and NIRSpec/G395H (one transit per instrument). We also combine the JWST observations with TESS and CHEOPS transit depths (Section 3.3). TOI-1130 b is a part of a rare multitransiting system, with an inner mini-Neptune (TOI-1130 b) and an outer hot Jupiter (TOI-1130 c). Such systems have a low occurrence rate of ~7%–8% among the hot Jupiter population (L. Sha et al. 2026), and cannot be formed through high-eccentricity migration (R. I. Dawson & J. A. Johnson 2018). The two planets are in a 2:1 mean motion resonance (J. Korth et al. 2023; L. Borsato et al. 2024), which indicates formation beyond the ice line and migration driven by disk interactions (P. Goldreich & S. Tremaine 1980). Interestingly, we note that the inner mini-Neptune lies at the edge of the so-called radius cliff, which is a sparsely populated part of the exoplanet radius–period space (A. Dattilo et al. 2023). The unique architecture of this system constrains its formation history, and allows us to test whether formation location and atmospheric composition are correlated.

We detect H_2O (7.5σ), CO_2 (3.3σ), and SO_2 (3.6σ), and a tentative detection of CH_4 (2σ) from the combined transmission spectrum (Figure 2). We used `PetitRadtrans` (P. Mollière et al. 2019) and `PLATON` (M. Zhang et al. 2020) to run free chemistry retrievals (Section 4.2). We find that the molecular detections and detected abundances are consistent within 1σ between the two independent retrieval frameworks (Table 2). We ran an equilibrium chemistry retrieval (Section 4.3) using `PetitRadtrans`. We constrained the atmospheric metallicity ($\log Z/Z_\odot = 1.8^{+0.4}_{-0.3}$) and a 3$\sigma$ upper limit to the C/O ratio (<0.75). We postprocess our samples to calculate the atmospheric μ ($5.5^{+1.3}_{-0.8}$ amu), confirming the volatile-rich nature of the atmosphere of this mini-Neptune. We run a grid of self-consistent forward models with `PICASO` (S. Mukherjee et al. 2023), and compare with the observed transmission spectrum of TOI-1130 b. We find a best-fit metallicity of 100 × solar and a C/O ratio of 0.3, consistent with the results from the equilibrium chemistry retrieval. The detection of SO_2, which is a photochemical product (S.-M. Tsai et al. 2023), also confirms the high metallicity of the atmosphere of this planet. SO_2 has been shown to be strongly dependent on atmospheric metallicity (I. J. M. Crossfield 2023), and its detection rules out solar-metallicity atmospheres (I. J. M. Crossfield et al. 2025; S. Mukherjee et al. 2025). We detect a slope in the optical part of the NIRISS/SOSS spectrum, which is consistent with the TESS and CHEOPS transit depths. The slope can be modeled using a Rayleigh or super-Rayleigh power-law model. However, haze models like Titan-like tholins, soot, and phosphorus hazes can be ruled out for this atmosphere at a >5σ level of confidence (Figure 4). We did not detect a significant He absorption signal in the NIRISS/SOSS transmission spectrum, and using `p-winds` models (L. A. Dos Santos et al. 2022) we can put an upper limit on the atmospheric escape rate ($<10^{11}$ g s^{-1}).

TOI-1130 b joins two other mini-Neptunes, TOI-270 d (B. Benneke et al. 2024) and GJ 3470 b (T. G. Beatty et al. 2024), with volatile-rich high-μ (5–6 amu) atmospheres. The μ for TOI-1130 b falls in between a pure H/H_e envelope and a pure steam envelope, and is consistent with an atmosphere where H/He and volatiles like H_2O are well mixed (miscible envelope mini-Neptune; B. Benneke et al. 2024). If we assume that this planet was born in situ, it would be difficult to explain its high volatile enrichment. At such close proximity to the star, the available solids are dominated by refractories. Although the gas phase can be enriched by migrating and evaporating pebbles, the presence of the hot Jupiter outside its orbit would cut off this supply, i.e., the so-called

pebble-filtering effect (B. Bitsch et al. 2021). Alternatively, if the planet was born beyond the ice line, it would have access to volatile-rich solids. It has been hypothesized that mini-Neptunes could have originated beyond the water ice line and been born with volatile-rich atmospheres and interiors (B. Bitsch et al. 2019; A. Aguichine et al. 2021). Therefore, the high μ we find for TOI-1130 b is consistent with formation beyond the ice line and agrees with the inferred formation scenario from its orbital architecture. If we assume that TOI-1130 b was born with a volatile-rich atmosphere, it is unlikely to have a significant mass or radius evolution (A. Aguichine et al. 2025; J. G. Rogers 2025). It has been shown that high-μ atmospheres could have low atmospheric escape (T. Yoshida & E. Gaidos 2025), which is consistent with the nondetection of a helium escape signal. Therefore, if we assume that this planet was born with a high-μ atmosphere, it could have maintained its original position in period–radius space at the end of its migration phase. This could potentially explain its location at the edge of the radius cliff. Furthermore, the detection of carbon-bearing molecules along with water is also consistent with formation beyond the ice line, as in situ formation models predict very low C/O ratios (M.-L. Steinmeyer et al. 2026).

The discovery of H/He-rich low mean molecular weight atmospheres of young sub-Neptunes (S. Barat et al. 2024b; P. C. Thao et al. 2024; S. Barat et al. 2025), the demographics of the small planet population (B. J. Fulton et al. 2017), and young transiting planets (S. Vach et al. 2024), evidence of atmospheric escape in mature mini-Neptunes (J. Orell-Miquel et al. 2024) provide evidence for the gas-dwarf in situ formation scenario for mini-Neptunes (J. G. Rogers 2025). However, the volatile-rich atmosphere of TOI-1130 b, along with its unique orbital architecture and position in the radius–period diagram provide evidence that mini-Neptunes do not have a homogeneous formation history, and ex situ volatile-rich formation mechanisms contribute to some fraction of their population (R. Burn et al. 2024; A. Chakrabarty et al. 2026).

Alternatively, it has been suggested that the source of volatiles in the atmospheres of mini-Neptunes could come from interior–atmosphere interactions (C. Dorn & T. Lichtenberg 2021; T. Lichtenberg et al. 2025). Although they have been shown to explain the volatile budget of low-mass mini-Neptunes like TOI-270 d (M. C. Nixon et al. 2025), it is unclear whether such large-scale magma oceans can exist for the more massive mini-Neptunes, like TOI-1130 b (B. Breza et al. 2025; R. Calder et al. 2025). Further theoretical investigation of interior structure models of mini-Neptunes is necessary to understand the extent to which interior–atmosphere interactions can alter the primordial composition of high-mass mini-Neptunes.

Acknowledgments

These observations are associated with program GO 3385. S.B. acknowledges the support for this program provided by NASA through a grant from the Space Telescope Science Institute, which is operated by the Association of Universities for Research in Astronomy, Inc., under NASA contract NAS 5-03127. C.X.H acknowledges that her research is sponsored by the Australian Research Council Future Fellowship FT240100016. G.Z. acknowledges that his research is sponsored by the Australian Research Council. CHEOPS is an ESA mission in partnership with Switzerland with important contributions to the payload and the ground segment from Austria, Belgium, France, Germany, Hungary, Italy, Portugal, Spain, Sweden, and the United Kingdom. The CHEOPS Consortium would like to gratefully acknowledge the support received by all the agencies, offices, universities, and industries involved. Their flexibility and willingness to explore new approaches were essential to the success of this mission. CHEOPS data analyzed in this Letter will be made available in the CHEOPS mission archive. The authors acknowledge support from the Swiss NCCR PlanetS and the Swiss National Science Foundation. This work has been carried out within the framework of the NCCR PlanetS supported by the Swiss National Science Foundation under grants 51NF40182901 and 51NF40205606. J.K. acknowledges support from the Swedish Research Council (Project Grants 2017-04945 and 2022-04043) and of the Swiss National Science Foundation under grant number TMSGI2_211697. H.P. acknowledges support by the Spanish Ministry of Science and Innovation with the Ramón y Cajal fellowship number RYC2021-031798-I. A.B. was supported by the Swedish National Space Agency. Funding from the University of La Laguna and the Spanish Ministry of Universities is acknowledged. ASTEP benefited from the support of the French and Italian polar agencies IPEV and PNRA in the framework of the Concordia station program.

Appendix A
JWST Data Reduction

A.1. NIRSpec Data Reduction

We start our data analysis from the uncalibrated 4D images downloaded from the MAST archive portal. We use the open-source JWST data analysis pipeline `Eureka!` (T. Bell et al. 2022) to analyze the images. In Stage 1 standard data reduction steps such as superbias correction, dark current subtraction, and jump detection during up-ramp sampling are applied using the standard `JWST` data reduction pipeline. We use a jump rejection threshold of 4σ. We test different values of the jump rejection threshold (3σ–6σ) and we found that the ultimate white light curve showed the minimum median absolute deviation (MAD) for 4σ. This step is effective in detecting cosmic rays. We also perform a crucial column-by-column median subtraction to account for the $1/f$ noise in the detector (N. Espinoza et al. 2023). It has been noted by multiple JWST/NIRSpec/G395H datasets where $1/f$ subtraction at the group level improves the final scatter in the white light curves by a factor of $\sim$2 (L. Alderson et al. 2023; E. M. May et al. 2023). We mask the trace while estimating the background in this step.

We extract 1D stellar spectra from the Stage 2 outputs from `Eureka!`. We first use the Stage 3 extraction routine from `Eureka!` itself. It first locates the trace on each column and fits a Gaussian profile to it. It corrects for the curvature of the trace on the detector and aligns all the columns. Then it applies an optimal extraction (K. Horne 1986). A column-by-column median background subtraction is applied in this stage as well. To estimate the weights for the optimal extraction it constructs a median image, which is smoothed spatially. Outlier rejection is applied both temporally and spatially to identify remnant cosmic rays and dead and hot pixels. The y- and x-position on the detector for both NRS1 and NRS2 are recorded during this stage. We do not find any signatures of mirror tilts or HGA

moves during the visit from the y-position time series. All the integrations are centered on the same pixel with an MAD of 0.01 in both the x- and y-direction. We use an aperture width of 8 pixels ensuring that the entire trace falls with the aperture window. Before the final light-curve extraction we visually inspect the stacked stellar spectra to look for any additional "bad columns." Such bad columns often appear as a vertical dark or bright line on the stacked stellar spectra. For the final light-curve extraction these columns are masked.

A.2. NIRISS/SOSS Data Reduction

The NIRISS/SOSS data analysis was carried out with the uncalibrated files. We use the `exoTEDRF` pipeline (M. Radica 2024) for the data reduction. We first proceed through the standard JWST data reduction steps such as superbias correction and reference pixel correction. We did not include the dark current subtraction step. The dark current is small and its reference file still contains residual $1/f$ noise (M. Radica 2024), which is why it introduces more noise in the images. We tested this by running reductions with and without a dark current subtraction step and found that including this step increases the scatter in the bluest part of the detector. For the subsequent analysis we turned off the dark current subtraction step. In NIRISS/SOSS the background is wavelength dependent (A. D. Feinstein et al. 2023) and must be subtracted before the group-level $1/f$ correction. The $1/f$ correction is applied using a column-by-column median subtraction and the subtracted background is readded. Following this in Stage 1, ramp fitting is done. In this step abrupt jumps at the group level can be identified.

In Stage 2, flat-field subtraction is done, the background is removed, and bad pixels are marked. We apply PCA to the time series at this stage. We remove the first three components of the PCA to remove detector-level effects. We find that removing more components did not decrease the MAD in the final white light curves. We note that an F227W image was not taken during these observations, so we skip the step where order-zero background contaminants are flagged.

We use the Stage 2 outputs to extract the 1D stellar spectra. We use a box half-width of 17 pixels centered on the trace of order 1 and order 2 on the detector. The box width is chosen such that all of the trace falls within the aperture. We do not see any significant overlap between order 1 and 2 and therefore apply simple box extraction. Using the ATOCA algorithm (M. Radica et al. 2022) to extract the 1D spectra did not significantly affect the extracted spectra and scatter in the white light curves.

Appendix B
Fitting the JWST Light Curves

B.1. NIRSpec Light-curve Analysis

We model the transit light curves using a linear baseline and the transit is modeled using a `batman` model (L. Kreidberg 2015). We fix the inclination, eccentricity, and orbital period from L. Borsato et al. (2024). We fit for the midtransit time, semimajor axis, quadratic limb darkening coefficients, transit depth, and a linear baseline. We used the MCMC sampler `emcee` (D. Foreman-Mackey et al. 2013) to sample the parameter space with 50 walkers each taking 5000 steps. The first 1000 steps are discarded as burn in. We find that

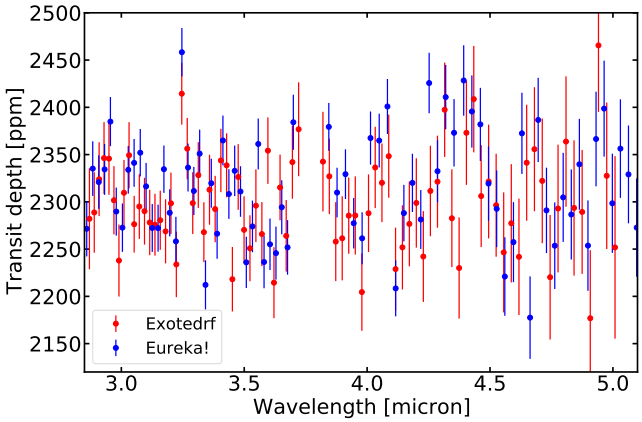


Figure B1. Comparison between NIRSpec/G395H transmission spectra of TOI-1130 b derived from independent data reductions from `Eureka!` and `exoTEDRF`. Light-curve fits were done using the common-mode method.

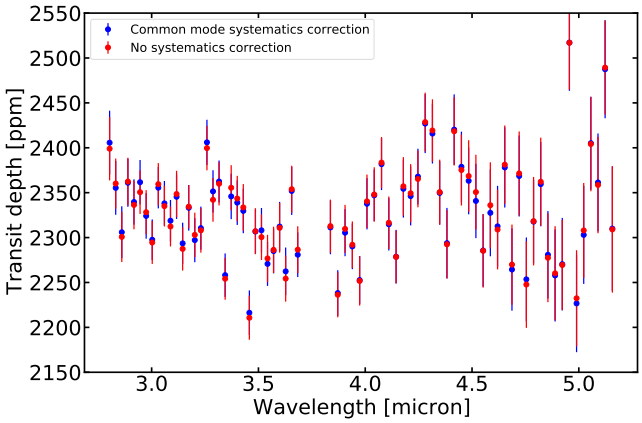


Figure B2. Comparison between NIRSpec/G395H transmission spectra of TOI-1130 b derived from independent light-curve analysis approaches: the common-mode technique and no additional systematics model. Light analysis done on `Eureka!` reduction.

the residuals in the white light curve shows some remaining red noise.

The spectroscopic light curves are fit using two methods: the same model as the white light curve, but we fix the midtransit time and semimajor axis from the respective white light curves. We also apply a common-mode (divide-white) method to detrend the spectroscopic light curves from wavelength-independent systematics. The common-mode method is useful whenever systematics can be considered wavelength independent (L. Kreidberg et al. 2014). We let the linear slope be free even for the common-mode-corrected light curves. This is done because the NRS1 slope is known to be wavelength dependent (e.g., see J. T. Sikora et al. 2025). The quadratic limb darkening coefficients are fixed from `Exotic-LD` (D. Grant & H. Wakeford 2024). The stellar parameters are taken from J. Korth et al. (2023). The temperature of TOI-1130 (4350 K) is in the sweet spot such that fixing the limb darkening does not introduce significant bias in the retrieved transit depths (N. Espinoza & A. Jordán 2015). We note that the residuals from the spectroscopic light-curve fits do not show any signs of red noise and bin down as expected for white noise. We note that the spectra derived from the independent data reductions yield consistent transmission spectra for both detectors (Figure B1). We also note that the

transmission spectra derived from both light-curve fitting approaches yield consistent results (Figure B2).

We also test the light-curve fits by leaving the midtransit time free. The spectrum is consistent with the fixed midtransit time case and the fitted midtransit times do not exhibit wavelength dependence. Recent observations of gas giants have shown that limb asymmetries can be quite common for these planets (M. M. Murphy et al. 2024; S. Mukherjee et al. 2025). One way to check for limb asymmetry is to fit the light curve using a symmetrical transit model like `batman`, but leave the midtransit time free. In case limb asymmetries are present they show wavelength-dependent features in the midtransit time spectrum (S. Mukherjee et al. 2025). However, given the signal-to-noise ratio (SNR) for a Neptune-size planet is lower than for a gas giant transit, we do not detect any limb asymmetry effect for this planet.

B.2. NIRISS Light-curve Analysis

The NIRISS/SOSSS white light curves (Figure 1) were analyzed similarly compared to the NIRSpec/G395H white light curves. The orbital parameters (inclination, eccentricity, and orbital period) were fixed to literature values from L. Borsato et al. (2024). The midtransit time, semimajor axis, quadratic limb darkening coefficients, transit depth, and a linear baseline were free parameters in the white light-curve fit. We used MCMC sampling implemented through `emcee` (D. Foreman-Mackey et al. 2013) to estimate the posterior distributions on these parameters. In the white light-curve residuals we can see a kink around 60546.56 MJD, which is likely due to a mirror tilt or HGA movement.

To account for this kink in the spectroscopic light curves, we take two approaches: first we remove all integrations before the kink to fit the spectroscopic light curves. Second, we apply a common-mode method where we derive a systematics model from the white light curve and by dividing the observed white light curve with the best-fit transit model. From the first fit we found that the linear slope of the baseline for both order 1 and order 2 do not show wavelength dependence. On visual inspection the detrended light curves from the common-mode correction do not show any residual features due to the kink. We also check that the spectroscopic light curves bin down consistently with white noise. Similar to the NIRSpec light curves, the quadratic limb darkening coefficients are fixed. The semimajor axis and midtransit times are fixed from the white light-curve fits. We also run a fit where we let the midtransit time be free for the spectroscopic light curves. We do not find significant wavelength dependence for the midtransit times, indicating that limb asymmetry effects are not significant in the NIRISS/SOSS bandpass.

A comparison between the spectrum derived from the brute force integration trimming approach and the common-mode correction method is shown in Figure B3. The extracted spectra and 1σ uncertainties are consistent between the two light-curve fitting approaches.

B.3. Transmission Spectrum Binning

The transmission spectra are derived by fitting the light curves at the native resolution. We derive the final transmission spectrum by binning the native-resolution transmission spectra. To decide the binning, we calculate the autocorrelation function (ACF) on the native-resolution transmission spectrum. For NIRISS order 1 and order 2 and NRS2 the ACF is sharply peaked at zero, but for NRS1 the ACF has nonzero values until 0.015 μm (Figure B4). We also calculate the Fourier transform of the native-resolution transmission spectrum of NRS1, which shows a sharp peak corresponding to 0.015 μm. We choose a bin width of 0.03 μm (50 pixels). This ensures that the Fourier transform of the bin has a value of zero at the peak of native-resolution spectrum Fourier transform. The other detectors do not show such features in the ACF or Fourier space. However, we still choose 50 pixel bins. Only for NIRISS/SOSS order 2 we choose only two bins since the SNR is low for this order.

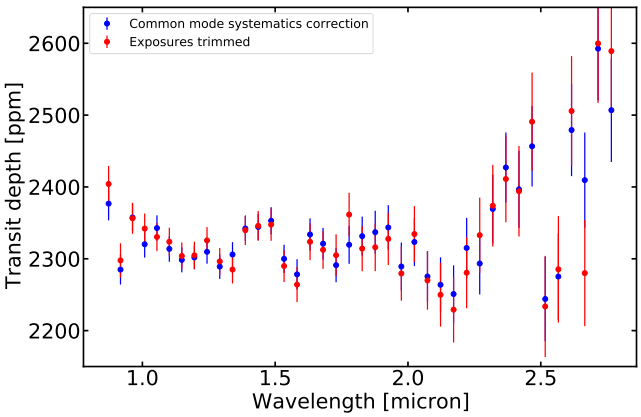


Figure B3. Comparison between the NIRISS/SOSS transmission spectrum of TOI-1130 b derived from independent light-curve analysis approaches: the common-mode technique and prekink exposures trimmed. Light analysis done on `exoTEDRF` reduction.

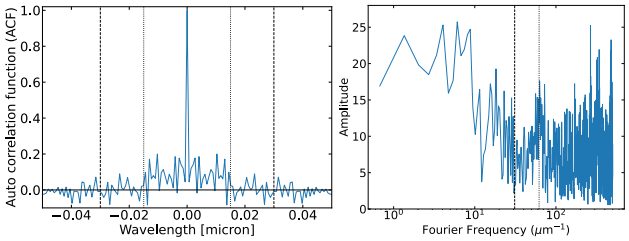


Figure B4. ACF (left) and Fourier transform (right) of the native-resolution spectrum derived from common-mode correction of the NRS1 light curves. The ACF shows nonzero values up to 0.015 μm (marked by a dotted vertical line). The corresponding Fourier frequency also shows a peak (dotted line). We choose a bin width of 50 pixels, which correspinds to twice the frequency of the peak. This ensures that Fourier transform of the binning function has a value of zero at the peak.

Appendix C
Atmospheric Retrievals of TOI-1130 b

C.1. `PetitRadtrans` *Free Retrieval*

We run a free chemistry retrieval on the transmission spectrum of TOI-1130 b (Figure 2). The retrieval is run on the combined TESS + CHEOPS + NIRISS/SOSS + NIRSpec/G395H spectrum. The NIRISS and NIRSpec spectra are binned at the 50 pixel level. A plane-parallel isothermal atmosphere is assumed. We choose a reference pressure of 0.01 bar. The radius at the reference pressure is a fitting parameter. The mass fractions of the included species are free parameters. The mass of the planet is fixed to 19.8 $M_\oplus$

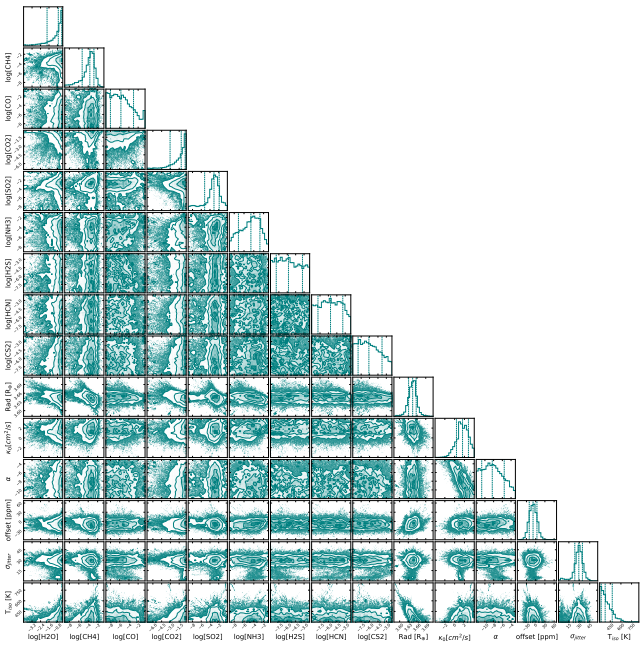


Figure C1. Posterior distributions from the free chemistry retrieval (Section 4.2) on the combined TESS, CHEOPS, and JWST transmission spectrum. The best-fit parameters are shown in Table 2.

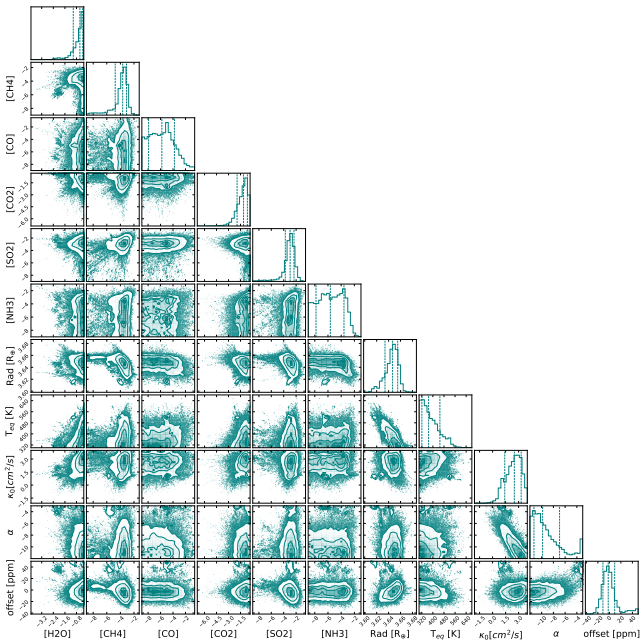


Figure C2. Posterior distributions from the free chemistry retrieval (Section 4.2) on the combined TESS, CHEOPS, and JWST transmission spectrum. We have removed the outliers between 2.3 and 2.7 μm for this retrieval. The best-fit parameters are shown in Table 2.

(L. Borsato et al. 2024). A power-law model is assumed for the aerosol opacity. We put uniform priors on all the fitting parameters. For the molecule mass fractions we use bounds from -10 to -0.2 in log space. We fit the transmission spectrum using an MCMC implemented through `emcee`. We use 50 walkers for 15,000 steps, with the first 3000 treated as a burn in. The retrieved posterior distributions from the free retrievals are shown in Figure C1. We have also run a free retrieval with NIRISS SOSS outliers removed (Figure C2) and by fixing the equilibrium temperature to 825 K (Figure C3).

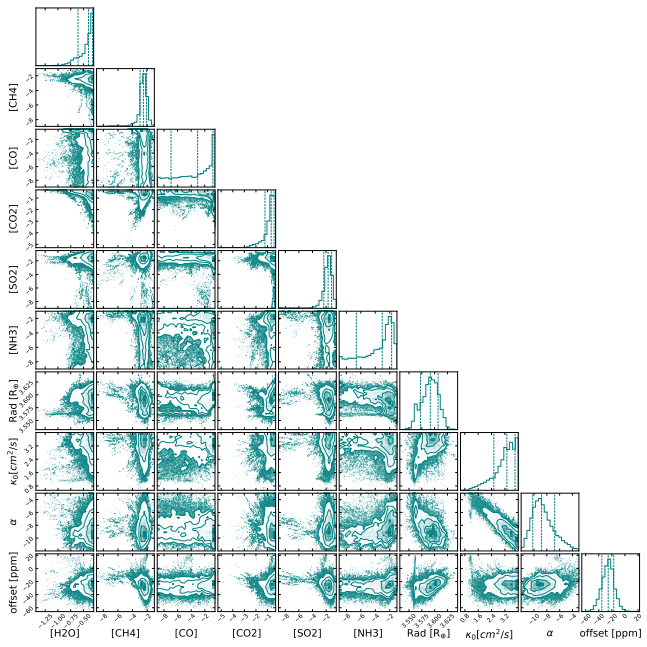


Figure C3. Posterior distributions from the free chemistry retrieval (Section 4.2) on the combined TESS, CHEOPS, and JWST transmission spectrum. We have fixed the isothermal temperature to 825 K (L. Borsato et al. 2024). The best-fit parameters are shown in Table 2.

We calculate the detection significances using a simple χ^2 difference. The χ^2 values are calculated for the best-fit model and a model where a particular molecule has been removed. Using χ^2 tables we convert the difference in χ^2 between the two models into a detection significance. In Table 1 we show the χ^2 values which were calculated for the different models.

We also calculate the Bayes factor to test the validity of the estimated detection significances. Bayes factors have been considered a benchmark for detection significances recently in the community (M. Holmberg & N. Madhusudhan 2023; S. Constantinou et al. 2026; D. P. Thorngren et al. 2026). We approximate the Bayes factor from the posterior distribution samples using the Savage–Dickey approximation (J. M. Dickey 1971). This approximation applies only if the null model is nested within the full model and the priors on the nuisance parameters remain unchanged for the null model (A. Mootoovaloo et al. 2016; J. Mulder et al. 2020). This approximation has been previously used for model comparisons in the context of exoplanets and retrievals (I. P. Waldmann et al. 2015; D. Kipping et al. 2024).

C.2. `PetitRadtrans` Equilibrium Chemistry Retrieval

We use the equilibrium chemistry module within `Petitradtrans` to calculate molecular abundances assuming equilibrium chemistry. It uses an equilibrium chemistry grid calculated using `EasyChem` (P. Mollière et al. 2017). It takes the atmospheric metallicity, C/O ratio, temperature, and pressure as input parameters and computes the abundances over the entire pressure range. For this retrieval we have assumed an isothermal atmosphere and included the temperature as a free parameter. We also include the metallicity and C/O ratio as free parameters. The results from the equilibrium chemistry retrievals are summarized in Table 3. The posterior distributions from the equilibrium fits are shown in Figures C4, C5, C6, and C7.

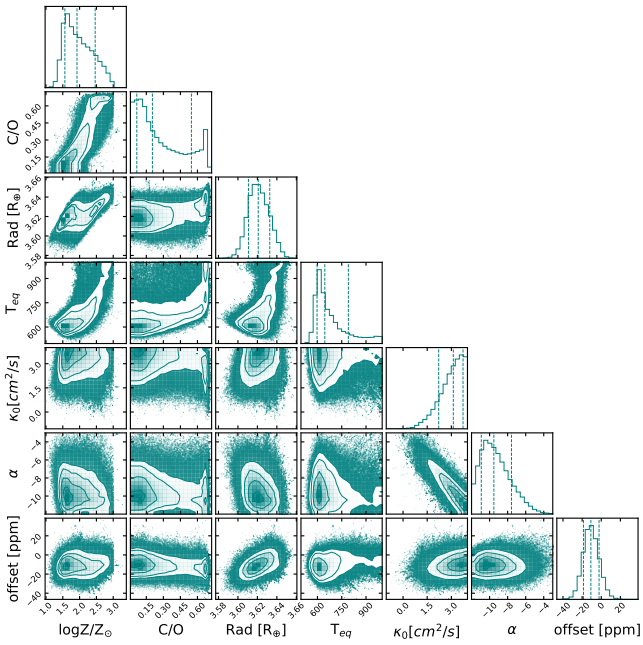


Figure C4. Posterior distributions from the equilibrium chemistry retrieval (Section 4.3) on the combined TESS, CHEOPS, and JWST transmission spectrum.

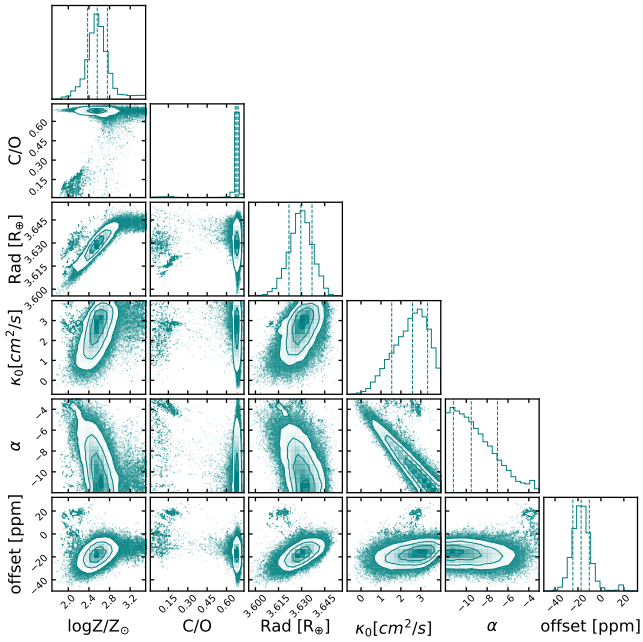


Figure C5. Posterior distributions from the equilibrium chemistry retrieval (Section 4.3) on the combined TESS, CHEOPS, and JWST transmission spectrum. The isothermal temperature is fixed to 825 K.

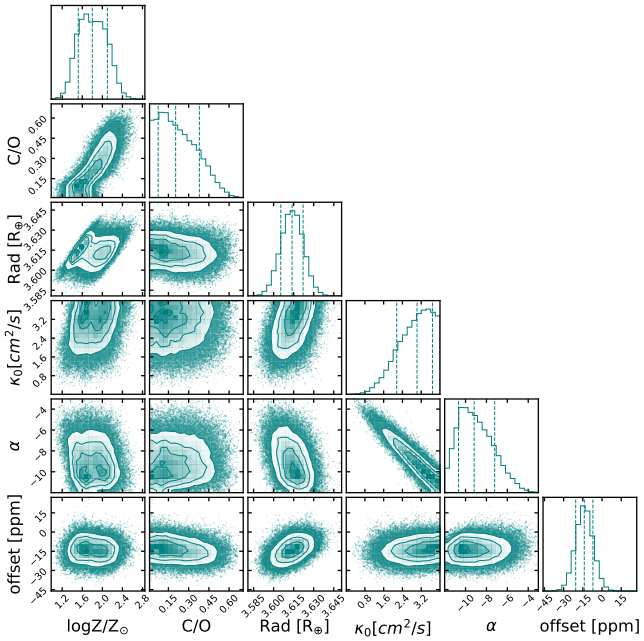


Figure C6. Posterior distributions from the equilibrium chemistry retrieval (Section 4.3) on the combined TESS, CHEOPS, and JWST transmission spectrum. The isothermal temperature is fixed to 625 K.

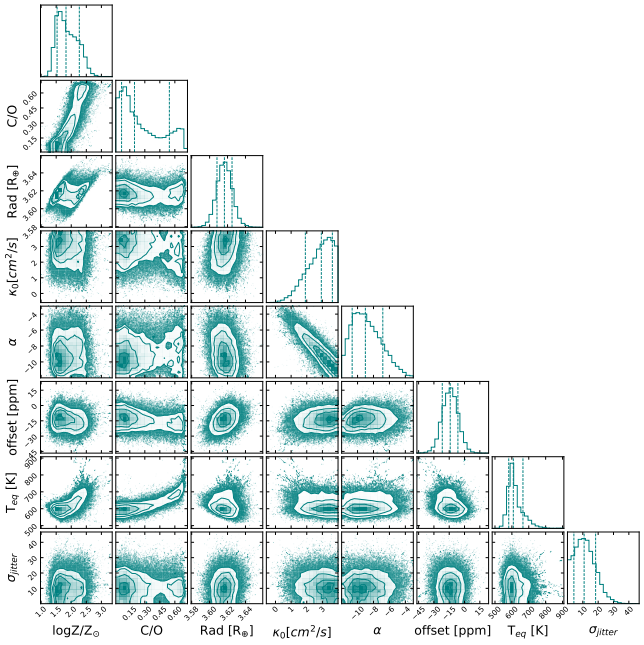


Figure C7. Posterior distributions from the equilibrium chemistry retrieval (Section 4.3) on the combined TESS, CHEOPS, and JWST transmission spectrum. We include a jitter term to account for residual red noise in the transmission spectrum.

Appendix D
Additional Tables

We list the data used to generate Figure 7 in Table D1 and the data for Figure 9 in Table D2.

Table D1
Table Showing the Radii, Temperature, and μ Values of the Sample of Planets Used to Generate Figure 7

Planet	Temperature (K)	Radius ($R_\oplus$)	μ (amu)	Reference(s)
K2-18 b	260	2.61	2.4^{+1}_{-1}	N. Madhusudhan et al. (2023), R. Liu et al. (2025)
TOI-270 d	373	2.13	$5.5^{+1.2}_{-1.1}$	(B. Benneke et al. 2024)
TOI-776 c	392	2.04	>7	(J. Teske et al. 2025)
GJ 1214 b	538	2.74	>10	(E. M. R. Kempton et al. 2023)
GJ 3470 b	650	3.88	$5.7^{+2}_{-1.5}$	(T. G. Beatty et al. 2024)
GJ 436 b	666	3.96	>6	(H. A. Knutson et al. 2014a)
TOI-836 c	626	2.58	>6	(N. L. Wallack et al. 2024)
GJ 3090 b	674	2.13	>6	(E.-M. Ahrer et al. 2025)
HAT-P-11 b	848	4.7	$2.3^{+0.3}_{-0.1}$	(Y. Chachan et al. 2019)
TOI-421 b	973	2.68	$2.3^{+1}_{-0.1}$	(B. Davenport et al. 2025)
HAT-P-26 b	970	6.3	2.5±0.3	(A. Gressier et al. 2025)

Table D2
Summary of Data Used to Generate Figure 9

Planet	T_{eq} (K)	R_p ($R_\oplus$)	$R_\star$ ($R_\odot$)	M_p ($M_\oplus$)	μ (amu)	$\Delta_{1.4}$ (ppm)	$\Delta_{1.2}$ (ppm)	$err_{1.4}$ (ppm)	$\Delta_{4.3}$ (ppm)	$\Delta_{4.1}$ (ppm)	$err_{4.1}$ (ppm)	References
K2-18 b	260	2.61	0.44	8.80	2.4	2945	2878	21	2960	2886	35	N. Madhusudhan et al. (2023)
TOI-270 d	373	2.13	0.38	4.78	5.5	2935	2825	13	3002	2870	45	B. Benneke et al. (2024)
TOI-776 c	392	2.05	0.54	7.00	7.0	…	…	…	1180	1140	30	J. Teske et al. (2025)
GJ 1214 b	538	2.74	0.21	8.40	10.0	13,522	13,495	27	135,056	135,121	60	E. M. R. Kempton et al. (2023)
HD 3167 c	546	3.01	0.86	9.80	4.0	955	909	11	…	…	…	T. Mikal-Evans et al. (2021)
GJ 3470 b	650	3.88	0.48	11.2	5.7	6122	5953	43	6109	5764	70	T. G. Beatty et al. (2024)
GJ 436 b	666	3.96	0.46	22.0	6.0	7036	7020	77	0	0	0	H. A. Knutson et al. (2014a)
TOI-674 b	676	5.25	0.42	23.00	4.0	13,195	13,110	72	…	…	…	J. Brande et al. (2022)
TOI-836 c	626	2.58	0.67	9.60	6.0	…	…	…	1220	1180	50	N. L. Wallack et al. (2024)
HD 97658 b	729	2.12	0.73	8.30	4.0	923	906	18	…	…	…	H. A. Knutson et al. (2014b)
GJ 3090 b	674	2.13	0.51	3.34	5.9	…	…	…	1540	1490	40	E.-M. Ahrer et al. (2025)
HAT-P-11 b	848	4.70	0.75	25.00	2.4	3498	3377	40	…	…	…	Y. Chachan et al. (2019)
HD 106315 c	1129	4.35	1.30	15.00	4.0	1099	1029	17	…	…	…	L. Kreidberg et al. (2022)
HIP 41378 b	985	2.90	1.40	8.30	4.0	395	373	17	…	…	…	B. Edwards et al. (2023)
TOI-421 b	973	2.68	0.87	7.00	2.33	…	…	…	820	640	40	B. Davenport et al. (2025)
HAT-P-26 b	970	6.30	0.79	19.00	2.5	5318	4912	45	5790	5250	50	A. Gressier et al. (2025)
HD 219666 b	1048	4.89	0.40	17.60	4.0	1833	1672	33	…	…	…	M. M. Murphy et al. (2025)

Note. For planets where JWST observations are available we have used those. For others we have used HST observations. For planets where μ is not constrained we have assumed $\mu = 4$ amu following J. Brande et al. (2024).

Appendix E
Log of Additional Observations of TOI-1130 b

We listed all TOI-1130 b observations used in addition to L. Borsato et al. (2024) and the JWST observations in Table E1.

Table E1
Additional TOI-1130 b Transits Used to Constraint the Transit Timing Model of the TOI-1130 System

#	Instrument/Observatory	Data ID	Start date (UTC)	Duration (hr)	No. of Frames	Exp. Time (s)
1	CHEOPS	CH_PR149003_TG000401_V0300	2024/08/24	10.86	421	60
2	TESS	tess2025180145000-s0094	2025/06/29	605.76	109,036	20
3	MINERVA	TOI-1130 b	2023/05/12	4.98	265	66
5	LCOGT	TIC254113311-02_20230517_LCO-SSO-1m0_ip	2023/05/17	6.9	543	15
6	LCOGT	TIC254113311-02_20230606_LCO-SAAO-1m0_ip	2023/06/06	6.65	529	15
7	LCOGT	TIC254113311-02_20230610_LCO-SAAO-1m0_ip	2023/06/10	5.58	448	45

Note. The CHEOPS and TESS data are also included in the global fit to provide the optical transit depth for the TOI-1130 b spectra.

ORCID iDs

Saugata Barat https://orcid.org/0009-0000-6113-0157
Tyler Fairnington https://orcid.org/0000-0002-0692-7822
Shelby Courreges https://orcid.org/0009-0002-9017-3679
Chelsea Huang https://orcid.org/0000-0003-0918-7484
Andrew Vanderburg https://orcid.org/0000-0001-7246-5438
Caroline V. Morley https://orcid.org/0000-0002-4404-0456
Judith Korth https://orcid.org/0000-0002-0076-6239
Hannu Parviainen https://orcid.org/0000-0001-5519-1391
Alexis Brandeker https://orcid.org/0000-0002-7201-7536
George Zhou https://orcid.org/0000-0002-4891-3517
Thomas M. Evans-Soma https://orcid.org/0000-0001-5442-1300
Lizhou Sha https://orcid.org/0000-0001-5401-8079
Douglas N. C. Lin https://orcid.org/0000-0001-5466-4628
Duncan Wright https://orcid.org/0000-0001-7294-5386
Ava Morrissey https://orcid.org/0009-0000-3527-8860
Emma Nabbie https://orcid.org/0000-0003-0571-2245
Karen A. Collins https://orcid.org/0000-0001-6588-9574
Phil Evans https://orcid.org/0000-0002-5674-2404
Tristan Guillot https://orcid.org/0000-0002-7188-8428
Keith Horne https://orcid.org/0000-0003-1728-0304
Don J. Radford https://orcid.org/0000-0002-3940-2360
Richard P. Schwarz https://orcid.org/0000-0001-8227-1020
Avi Shporer https://orcid.org/0000-0002-1836-3120
Olga Suarez https://orcid.org/0000-0002-3503-3617

References

Aguichine, A., Batalha, N., Fortney, J. J., et al. 2025, ApJ, 988, 186
Aguichine, A., Mousis, O., Deleuil, M., & Marcq, E. 2021, ApJ, 914, 84
Ahrer, E.-M., Radica, M., Piaulet-Ghorayeb, C., et al. 2025, ApJL, 985, L10
Alderson, L., Wakeford, H. R., Alam, M. K., et al. 2023, Natur, 614, 664
Alderson, L., Moran, S. E., Wallack, N. L., et al. 2025, AJ, 169, 142
Barat, S., Désert, J.-M., Vazan, A., et al. 2024a, NatAs, 8, 899
Barat, S., Désert, J.-M., Goyal, J. M., et al. 2024b, A&A, 692, A198
Barat, S., Désert, J.-M., Mukherjee, S., et al. 2025, AJ, 170, 165
Batalha, N. E., Marley, M. S., Lewis, N. K., & Fortney, J. J. 2019, ApJ, 878, 70
Batalha, N. E., Mandell, A., Pontoppidan, K., et al. 2017, PASP, 129, 064501
Batalha, N. E., Rooney, C. M., Visscher, C., et al. 2026, AJ, 171, 98
Batygin, K., Bodenheimer, P. H., & Laughlin, G. P. 2016, ApJ, 829, 114
Beatty, T. G., Welbanks, L., Schlawin, E., et al. 2024, ApJL, 970, L10
Beaugé, C., Michtchenko, T. A., & Ferraz-Mello, S. 2006, MNRAS, 365, 1160
Becker, J. C., Vanderburg, A., Adams, F. C., Rappaport, S. A., & Schwengeler, H. M. 2015, ApJL, 812, L18
Bell, T., Ahrer, E.-M., Brande, J., et al. 2022, JOSS, 7, 4503
Benneke, B., Roy, P.-A., Coulombe, L.-P., et al. 2024, arXiv:2403.03325
Benz, W., Broeg, C., Fortier, A., et al. 2021, ExA, 51, 109
Bitsch, B., Morbidelli, A., Johansen, A., et al. 2018, A&A, 612, A30
Bitsch, B., Raymond, S. N., Buchhave, L. A., et al. 2021, A&A, 649, L5
Bitsch, B., Raymond, S. N., & Izidoro, A. 2019, A&A, 624, A109
Booth, R. A., Clarke, C. J., Madhusudhan, N., & Ilee, J. D. 2017, MNRAS, 469, 3994
Borsato, L., Degen, D., Leleu, A., et al. 2024, A&A, 689, A52
Brande, J., Crossfield, I. J. M., Kreidberg, L., et al. 2022, AJ, 164, 197
Brande, J., Crossfield, I. J. M., Kreidberg, L., et al. 2024, ApJL, 961, L23
Brandeker, A., Patel, J. A., & Morris, B. M. 2024, PIPE: Extracting PSF photometry from CHEOPS data, Astrophysics Source Code Library, record, ascl:2404.002
Brandeker, A., Heng, K., Lendl, M., et al. 2022, A&A, 659, L4
Breza, B., Nixon, M. C., & Kempton, E. M.-R. 2025, ApJL, 993, L46
Burn, R., Mordasini, C., Mishra, L., et al. 2024, NatAs, 8, 463
Calder, R., Shorttle, O., Nicholls, H., Lichtenberg, T., & Guimond, C.-M. 2025, arXiv:2512.05816
Chachan, Y., Knutson, H. A., Gao, P., et al. 2019, AJ, 158, 244
Chakrabarty, A., Mulders, G. D., Aguichine, A., & Batalha, N. 2026, ApJ, 999, 188
Chatterjee, S., Ford, E. B., Matsumura, S., & Rasio, F. A. 2008, ApJ, 686, 580
Constantinou, S., Madhusudhan, N., & Holmberg, M. 2026, A&A, 705, A25
Crossfield, I. J. M. 2023, ApJL, 952, L18
Crossfield, I. J. M., Ahrer, E.-M., Brande, J., et al. 2025, ApJ, 994, 184
Dattilo, A., & Batalha, N. M. 2024, AJ, 167, 288
Dattilo, A., Batalha, N. M., & Bryson, S. 2023, AJ, 166, 122
Davenport, B., Kempton, E. M. R., Nixon, M. C., et al. 2025, ApJL, 984, L44
Dawson, R. I., & Johnson, J. A. 2018, ARA&A, 56, 175
de Wit, J., & Seager, S. 2013, Sci, 342, 1473
Dickey, J. M. 1971, AnnMS, 42, 204
Dorn, C., & Lichtenberg, T. 2021, ApJL, 922, L4
Dos Santos, L. A., Vidotto, A. A., Vissapragada, S., et al. 2022, A&A, 659, A62
Edwards, B., Changeat, Q., Tsiaras, A., et al. 2023, ApJS, 269, 31
Espinoza, N., & Jordán, A. 2015, MNRAS, 450, 1879
Espinoza, N., Úbeda, L., Birkmann, S. M., et al. 2023, PASP, 135, 018002
Feinstein, A. D., Radica, M., Welbanks, L., et al. 2023, Natur, 614, 670
Feinstein, A. D., Booth, R. A., Bergner, J. B., et al. 2025, arXiv:2506.00669
Foreman-Mackey, D., Hogg, D. W., Lang, D., & Goodman, J. 2013, PASP, 125, 306
Fortney, J. J., Dawson, R. I., & Komacek, T. D. 2021, JGRE, 126, e06629
Fortney, J. J., Visscher, C., Marley, M. S., et al. 2020, AJ, 160, 288

France, K., Loyd, R. O. P., Youngblood, A., et al. 2016, ApJ, 820, 89
Fulton, B. J., Petigura, E. A., Howard, A. W., et al. 2017, AJ, 154, 109
Gao, P., & Zhang, X. 2020, ApJ, 890, 93
Gao, P., Thorngren, D. P., Lee, E. K. H., et al. 2020, NatAs, 4, 951
Gibson, N. P., Aigrain, S., Barstow, J. K., et al. 2013, MNRAS, 428, 3680
Ginzburg, S., Schlichting, H. E., & Sari, R. 2018, MNRAS, 476, 759
Goldreich, P., & Tremaine, S. 1980, ApJ, 241, 425
Grant, D., & Wakeford, H. 2024, JOSS, 9, 6816
Grant, D., Lewis, N. K., Wakeford, H. R., et al. 2023, ApJL, 956, L32
Gressier, A., Batalha, N. E., Wogan, N., et al. 2025, AJ, 170, 292
Guillot, T., Abe, L., Agabi, A., et al. 2015, AN, 336, 638
Gupta, A., & Schlichting, H. E. 2019, MNRAS, 487, 24
Haugbølle, T., Weber, P., Wielandt, D. P., et al. 2019, AJ, 158, 55
He, C., Hörst, S. M., Lewis, N. K., et al. 2018, ApJL, 856, L3
He, C., Hörst, S. M., Lewis, N. K., et al. 2018, AJ, 156, 38
Hoch, K. K. W., Rowland, M., Petrus, S., et al. 2025, Natur, 643, 938
Holmberg, M., & Madhusudhan, N. 2023, MNRAS, 524, 377
Horne, K. 1986, PASP, 98, 609
Hoyer, S., Guterman, P., Demangeon, O., et al. 2020, A&A, 635, A24
Hsu, D. C., Ford, E. B., Ragozzine, D., & Ashby, K. 2019, AJ, 158, 109
Huang, C., Wu, Y., & Triaud, A. H. M. J. 2016, ApJ, 825, 98
Huang, C. X., Quinn, S. N., Vanderburg, A., et al. 2020a, ApJL, 892, L7
Huang, C. X., Vanderburg, A., Pál, A., et al. 2020b, RNAAS, 4, 204
Huang, C. X., Vanderburg, A., Pál, A., et al. 2020c, RNAAS, 4, 206
Ida, S., & Lin, D. N. C. 2008, ApJ, 673, 487
Inglis, J., Batalha, N. E., Lewis, N. K., et al. 2024, ApJL, 973, L41
Johansen, A., & Lambrechts, M. 2017, AREPS, 45, 359
Kawashima, Y., & Ikoma, M. 2018, ApJ, 853, 7
Kempton, E. M. R., Zhang, M., Bean, J. L., et al. 2023, Natur, 620, 67
Khare, B. N., Sagan, C., Arakawa, E. T., et al. 1984, Icar, 60, 127
Khare, B. N., Thompson, W. R., Cheng, L., et al. 1993, Icar, 103, 290
Khorshid, N., Min, M., Désert, J. M., Woitke, P., & Dominik, C. 2022, A&A, 667, A147
Kipping, D., Teachey, A., Yahalomi, D. A., et al. 2024, arXiv:2401.10333
Kite, E. S., Fegley, B., Jr., Schaefer, L., & Ford, E. B. 2020, ApJ, 891, 111
Knutson, H. A., Benneke, B., Deming, D., & Homeier, D. 2014a, Natur, 505, 66
Knutson, H. A., Dragomir, D., Kreidberg, L., et al. 2014b, ApJ, 794, 155
Korth, J., Gandolfi, D., Šubjak, J., et al. 2023, A&A, 675, A115
Kreidberg, L. 2015, PASP, 127, 1161
Kreidberg, L., Bean, J. L., Désert, J.-M., et al. 2014, Natur, 505, 69
Kreidberg, L., Mollière, P., Crossfield, I. J. M., et al. 2022, AJ, 164, 124
Lavvas, P., & Koskinen, T. 2017, ApJ, 847, 32
Lee, E. J., & Chiang, E. 2016, ApJ, 817, 90
Lee, E. J., Chiang, E., & Ormel, C. W. 2014, ApJ, 797, 95
Lee, E. J., & Owen, J. E. 2025, ApJL, 980, L40
Lichtenberg, T., Shorttle, O., Teske, J., & Kempton, E. M.-R. 2025, Sci, 390, eads3660
Lin, D. N. C., Bodenheimer, P., & Richardson, D. C. 1996, Natur, 380, 606
Liu, R., Lavvas, P., Tinetti, G., et al. 2025, arXiv:2509.10947
MacDonald, R. J., Goyal, J. M., & Lewis, N. K. 2020, ApJL, 893, L43
Madhusudhan, N., Holmberg, M., Constantinou, S., & Cooke, G. J. 2025, arXiv:2509.19247
Madhusudhan, N., Sarkar, S., Constantinou, S., et al. 2023, ApJL, 956, L13
Marley, M. S., Saumon, D., Visscher, C., et al. 2021, ApJ, 920, 85
Maxted, P. F. L., Ehrenreich, D., Wilson, T. G., et al. 2022, MNRAS, 514, 77
May, E. M., MacDonald, R. J., Bennett, K. A., et al. 2023, ApJL, 959, L9
Mayo, A. W., Fortenbach, C. D., Louie, D. R., et al. 2025, AJ, 170, 50
Mayor, M., & Queloz, D. 1995, Natur, 378, 355
Mikal-Evans, T., Crossfield, I. J. M., Benneke, B., et al. 2021, AJ, 161, 18
Miles, B. E., Biller, B. A., Patapis, P., et al. 2023, ApJL, 946, L6
Mollière, P., van Boekel, R., Bouwman, J., et al. 2017, A&A, 600, A10
Mollière, P., Wardenier, J. P., van Boekel, R., et al. 2019, A&A, 627, A67
Mollière, P., Molyarova, T., Bitsch, B., et al. 2022, ApJ, 934, 74
Mootoovaloo, A., Bassett, B. A., & Kunz, M. 2016, arXiv:1609.02186
Mukherjee, S., Batalha, N. E., Fortney, J. J., & Marley, M. S. 2023, ApJ, 942, 71
Mukherjee, S., Fortney, J. J., Wogan, N. F., Sing, D. K., & Ohno, K. 2025, ApJ, 985, 209
Mukherjee, S., Sing, D. K., Fu, G., et al. 2025, arXiv:2505.10910
Mulder, J., Wagenmakers, E. J., & Marsman, M. 2020, arXiv:2004.09899
Murphy, M. M., Beatty, T. G., Welbanks, L., & Fu, G. 2025, AJ, 169, 286
Murphy, M. M., Beatty, T. G., Schlawin, E., et al. 2024, NatAs, 8, 1562
Mustill, A. J., Davies, M. B., & Johansen, A. 2015, ApJ, 808, 14
Naoz, S. 2016, ARA&A, 54, 441
Nixon, M. C., Somers, R. S., Savel, A. B., et al. 2025, ApJ, 995, 95
Norfolk, B. J., Maddison, S. T., Pinte, C., et al. 2021, MNRAS, 502, 5779
Noy, N., Podolak, M., & Bar-Nun, A. 1981, JGRC, 86, 11985
Öberg, K. I., Murray-Clay, R., & Bergin, E. A. 2011, ApJL, 743, L16
Oklopčić, A., & Hirata, C. M. 2018, ApJL, 855, L11
Orell-Miquel, J., Murgas, F., Pallé, E., et al. 2024, A&A, 689, A179
Owen, J. E., & Jackson, A. P. 2012, MNRAS, 425, 2931
Owen, J. E., & Schlichting, H. E. 2024, MNRAS, 528, 1615
Owen, J. E., & Wu, Y. 2013, ApJ, 775, 105
Owen, J. E., & Wu, Y. 2016, ApJ, 817, 107
Owen, J. E., & Wu, Y. 2017, ApJ, 847, 29
Penzlin, A. B. T., Booth, R. A., Kirk, J., et al. 2024, MNRAS, 535, 171
Pollack, J. B., Hubickyj, O., Bodenheimer, P., et al. 1996, Icar, 124, 62
Radica, M. 2024, JOSS, 9, 6898
Radica, M., Albert, L., Taylor, J., et al. 2022, PASP, 134, 104502
Radica, M., Piaulet-Ghorayeb, C., Taylor, J., et al. 2025, ApJL, 979, L5
Raymond, S. N., Boulet, T., Izidoro, A., Esteves, L., & Bitsch, B. 2018, MNRAS, 479, L81
Rigby, F. E., Madhusudhan, N., Sarkar, S., et al. 2025, ApJL, 995, L70
Rigby, F. E., Pica-Ciamarra, L., Holmberg, M., et al. 2024, ApJ, 975, 101
Rogers, J. G. 2025, MNRAS, 539, 2230
Schlichting, H. E. 2014, ApJL, 795, L15
Schneider, A. D., & Bitsch, B. 2021, A&A, 654, A71
Sha, L., Vanderburg, A. M., Huang, C. X., et al. 2023, MNRAS, 524, 1113
Sha, L., Vanderburg, A. M., Huang, C. X., et al. 2026, arXiv:2601.13302
Shorttle, O., Jordan, S., Nicholls, H., Lichtenberg, T., & Bower, D. J. 2024, ApJL, 962, L8
Sikora, J. T., Rowe, J. F., Splinter, J., et al. 2025, AJ, 170, 105
Smith, J. C., Stumpe, M. C., Van Cleve, J. E., et al. 2012, PASP, 124, 1000
Spake, J. J., Sing, D. K., Evans, T. M., et al. 2018, Natur, 557, 68
Steinmeyer, M.-L., Dorn, C., Werlen, A., & Grimm, S. L. 2026, ApJ, 1001, 36
Stevenson, K. B., Bean, J. L., Seifahrt, A., et al. 2014, AJ, 147, 161
Stumpe, M. C., Smith, J. C., Catanzarite, J. H., et al. 2014, PASP, 126, 100
Stumpe, M. C., Smith, J. C., Van Cleve, J. E., et al. 2012, PASP, 124, 985
Sumlin, B. J., Heinson, W. R., & Chakrabarty, R. K. 2018, JQSRT, 205, 127
Teske, J., Batalha, N. E., Wallack, N. L., et al. 2025, AJ, 169, 249
Thao, P. C., Mann, A. W., Feinstein, A. D., et al. 2024, AJ, 168, 297
Thorngren, D. P., Sing, D. K., & Mukherjee, S. 2026, ApJS, 283, 10
Trotta, R. 2008, ConPh, 49, 71
Tsai, S.-M., Lee, E. K. H., Powell, D., et al. 2023, Natur, 617, 483
Vach, S., Zhou, G., Huang, C. X., et al. 2024, AJ, 167, 210
Venturini, J., Guilera, O. M., Haldemann, J., Ronco, M. P., & Mordasini, C. 2020, A&A, 643, L1
Waldmann, I. P., Tinetti, G., Rocchetto, M., et al. 2015, ApJ, 802, 107
Wallack, N. L., Batalha, N. E., Alderson, L., et al. 2024, AJ, 168, 77
Werlen, A., Dorn, C., Burn, R., et al. 2025a, ApJL, 991, L16
Werlen, A., Dorn, C., Schlichting, H. E., Grimm, S. L., & Young, E. D. 2025b, ApJL, 988, L55
Wogan, N. F., Batalha, N. E., Zahnle, K., et al. 2024, ApJL, 963, L7
Wogan, N. F., Catling, D. C., Zahnle, K. J., & Lupu, R. 2023, PSJ, 4, 169
Wu, Y., & Murray, N. 2003, ApJ, 589, 605
Yoshida, T., & Gaidos, E. 2025, A&A, 696, L13
Yu, X., He, C., Zhang, X., et al. 2021, NatAs, 5, 822
Zeng, L., Jacobsen, S. B., Hyung, E., et al. 2021, ApJ, 923, 247
Zhang, M., Chachan, Y., Kempton, E. M. R., Knutson, H. A., & Chang, W. H. 2020, ApJ, 899, 27
Zhang, M., Paragas, K., Bean, J. L., et al. 2025, AJ, 169, 38
Zhu, Z., Nelson, R. P., Dong, R., Espaillat, C., & Hartmann, L. 2012, ApJ, 755, 6